ALMA MATER STUDIORUM — UNIVERSITÀ DI BOLOGNA

SCUOLA DI SCIENZE
Corso di Laurea Magistrale in Astrofisica e Cosmologia
Dipartimento di Fisica e Astronomia

Constraining the Initial Mass Function of the giant Early-Type Galaxies NGC 1332 and NGC 7619

Tesi di Laurea Magistrale

Candidato:
Matteo Vignola

Relatore:
Chiar.mo Prof.
Andrea Cimatti

Co-relatori:
P.D. Dr. Roberto Saglia
Dr. Matteo Fossati
Dr. Alessandra Beifiori

Sessione III
Anno Accademico 2016-2017

To my grandmothers

Abstract

La funzione di massa iniziale (IMF) descrive la distribuzione delle masse per una popolazione di stelle al momento della sua formazione. Caretterizzare questa distribuzione è quindi cruciale per comprendere la fisica dei processi di formazione stellare. Le assunzioni sulla forma della IMF hanno un significativo impatto su numerose proprietà fisiche, quali la storia di formazione delle galassie, il loro rapporto massa-luminosità e sono fondamentali per una stima accurata della masse stellari. Le forme più usate per questa funzione sono le parametrizzazioni dette di Salpeter o di Kroupa, che differiscono per un diverso rapporto tra stelle a grande massa rispetto a quelle a bassa massa. Nonostante il suo ruolo centrale in molte aree dell'astrofisica, un teora fisica completa che spieghi la forma dell'IMF è ancora mancante. La IMF è stata per molto tempo considerata universale (invariante nello spazio e nel tempo), poichè nella Via Lattea non ci sono evidenti variazioni. Ciononostante, diversi studi ne teorizzano o osservano una variazione (Conroy & van Dokkum 2012), ed il dibatto sulle variabili fisiche che la influenzano, come anche quello sulla loro interazione, è apertissimo. Nelle galassie Early-Type più massiccie, diversi studi (Conroy & van Dokkum 2012; Thomas et al. 2011; Cappellari 2012) mostrano che la forma della IMF varia in funzione della dispersione di velocità delle stelle. In particolare, nelle galassie con alta dispersione di velocità si osserva un numero di stelle a bassa massa anche maggiore di quanto atteso dalla IMF di Salpeter (Conroy et al. 2013).

In questo lavoro , sono state studiate due galassie Early-Type, NGC 1332 and NGC 7619, con l'obiettivo di investigare eventuali variazioni radiali nella loro IMF. Questo studio è stato possibile grazie ad osservazioni eseguite tramite due strumenti di spettroscopia a campo integrale, KMOS e MUSE, entrambi montati sul Very Large Telescope, in Cile.

Sulla base di queste osservazioni abbiamo potuto eseguire uno studio cinematico dettagliato delle sorgenti, utilizzando il codice pPXF (Cappellari & Emsellem 2004), derivando le distribuzioni di velocità lungo la linea di vista per entrambe le galassie. I risultati cinematici ottenuti sia riguardo le velocità di rotazione che riguardo la dispersione di velocità si sono dimostrati consistenti con i precedenti studi a riguardo (Pu et al. 2010; Rusli et al. 2011).

Grazie ai parametri cinematici ottenuti, abbiamo sviluppato un codice in grado misurare gli indici di Lick per le righe di assorbimento di interesse (*Hbeta*, *Mg*, *CaII*1, *CaII*2, *CaII*3, *Hbeta*, *Mgb*, *Fe*5015, *Fe*5270, *Fe*5335,*Fe*5406, *Fe*5709, *Fe*5782, *NaI*,*NaD*) in modo da poter ricostruire le proprietà fisiche delle galassie in esame. Il codice utilizzato è progettato per tenere conto dell'allargamento delle righe dovuto alla dispersione di velocità rispetto alle definizioni di Lick, che corrispondono a 220 km s^{-1}. Per ottenere incertezze affidabili sulle misure il codice fa uso di una simulazione MonteCarlo. Per via della bassa sensibilita' di KMOS a luce nella banda IZ dove sono state effettuate le osservazioni, gli spettri derivati da questi dati non hanno un rapporto segnale rumore sufficientemente alto da permettere di misurarne le righe di assorbimento in maniera attendibile.

Abbiamo poi interpretato queste misure tramite tre differenti modelli di popolazioni stellari. Il primo modello utilizzato (Thomas et al. 2005) presenta una parametrizzazione della IMF di tipo Kroupa fissa, ma età, metallicità, M/L e α/Fe variabili. Il secondo modello (Conroy et al. 2009) presenta invece una abbondanza fissa sul valore solare rispetto al primo, permettendo però di variare la forma della IMF. Infine, il terzo modello Conroy & van Dokkum (2012), per un'età fissata a 13.5 Gyr e metallicità solare consente di studiare l'impatto di un differente rapporto α/Fe.

Dallo questo studio comparato abbiamo ottenuto due galassie vecchie, ricche di metalli e sovrabbondanti rispetto ai valori solari, in accordo coi precedenti lavori su NGC 1332 Rusli et al. (2011) e su NGC 7619 (Rusli et al. 2013). Abbiamo quindi potuto osservare una forte dipendenza dell'indice *NaI* alla pendenza della IMF nel regime delle stelle nane ($0.08M_{\odot} < M < 0.5M_{\odot}$) , anche se i valori misurati variano significativamente sia in funzione della metallicità che della sovra-abbondanza.

Per proseguire in questo studio, saranno quindi necessari nuovi modelli di popolazioni stellari che ci permettano di parametrizzare contemporaneamente metallicità, sovra-abbondanza α/Fe, età e forma della IMF. In conclusione, una ricostruzione accurata della forma della IMF vincolerà fortemente la dipendenza radiale del rapporto massa-luminosità, un parametro di importanza vitale per i modelli dinamici di galassie di questo tipo, grazie ai quali ricostruire statisticamente le orbite delle stelle. Queste ultime potranno poi essere comparate ad osservazioni spettroscopiche e fotometriche, contribuendo alla stima del ruolo della materia oscura e dei buchi neri nelle regioni centrali delle galassie Early-Type.

Contents

List of Figures

List of Tables

Chapter 1

Introduction

1.1 Galaxies

Galaxies are the building blocks of the Universe. They are gravitationally bound systems, mainly composed in terms of baryonic matter in form of stars, gas and dust. Galaxies are inhomogeneously distributed within the Universe, they in fact tending to aggregate in groups, filaments and clusters that can reach a mass up to $10^{15} M_{\odot}$. It is common belief today, that most (if not all) galaxies present a super-massive black hole in their center, whose evolution has deeply affected the one of the entire system. Spanning a wide range in sizes, masses and morphologies, and involving many physical processes, galaxies play a pivotal role in the study of the structure and evolution of the Universe.

Galaxies have been morphologically classified by Hubble (*Realm of Nebulae*, 1936) into ellipticals and spirals. Later on, Irregulars have been added to the diagram by De Vaucouleurs in 1959, as one can see in Figure1.1. Elliptical galaxies (on the left side of the diagram) are usually brighter and more massive (with a mass range from 10^5 to $10^{13} M_{\odot}$) than spirals and have a spheroidal shape. They are further classified according to their ellipticity, the ratio between the minor axis and the major one. This ratio vary from 0 to 0.7 from which we have seven categories for elliptical galaxies, *Ek* from E0 to E7, where $k = 10 * (1 - b/a)$. Being a and b the major and minor axis. Their colors usually tend to be redder than those of spirals, identifying them as older and without any on-going star formation process. This work is focused on this type of galaxies.

Spiral galaxies (on the two arms of the diagram in Figure1.1) instead, present a characteristic disk shape, and have been morphologically classified first of all by the shape of their inner bulge, that could be spheroidal (S) or barred (Sb). Then spirals are morphologically classified depending on the winding of their arms, that give them indeed their spiral shape: from a tighter winding of the arms(Sa

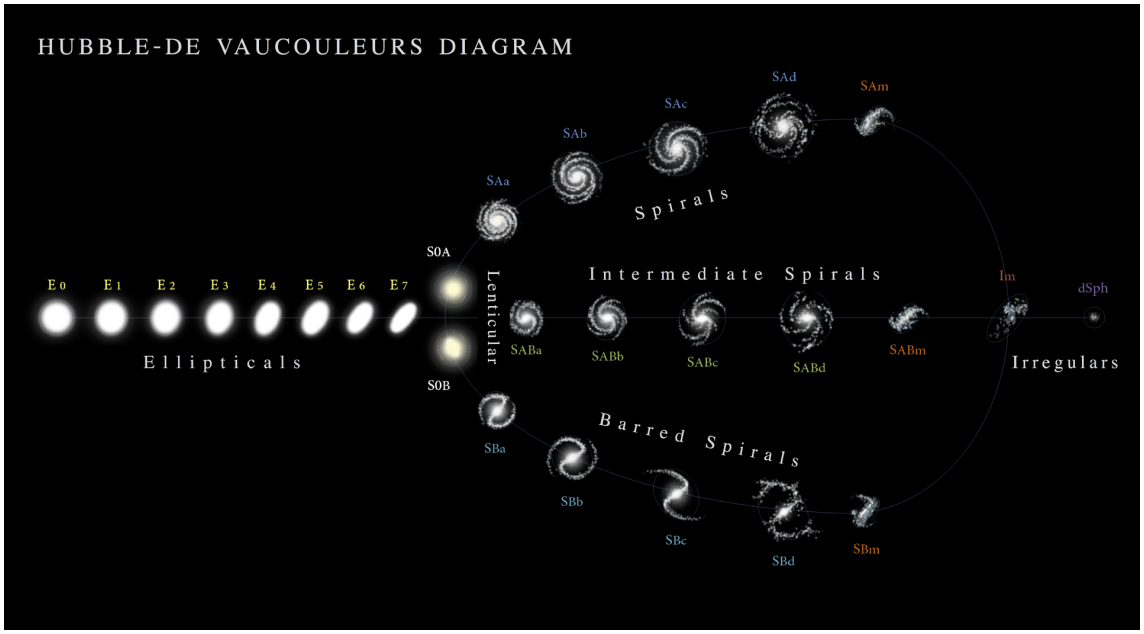

Figure 1.1: Hubble - De Vaucoulers galaxies classification [Credit:Antonio Ciccolella / M. De Leo]

or Sba) to the most wider one (Sc o Sbc). Spiral galaxies are often areas of star formation processes, especially in their arms, while their pseudo/central bulge presents proprieties more similar to ellipticals.

Between ellipticals and spirals in Figure1.1, lenticular galaxies (S0) are found. They represent the connection among the two galaxies types, since they present a central bulge spiral like, but they do not have spiral arms. Finally, there are Irregulars galaxies (Irr, at the right side of the sequence). These are amorphous, gas rich and they host intensive star formation activity.

1.2 Elliptical galaxies

As already mentioned, elliptical galaxies present red photometric colours, characteristic of an old, metal-rich stellar population. Typically they do not present a prominent star formation processes, they contain little cold gas and dust, and their surface brightness distribution is smooth. The average surface distribution is:

$$\langle I_e \rangle = \frac{L}{2\pi R_e^2} \tag{1.1}$$

Where L is the total luminosity and R_e is the effective radius, defined as the radius at which half of the total light of the system is emitted.

In elliptical galaxies it is possible to define different isophotal shapes. The latter may change with radius, causing a phenomenon called isophote twisting. The main two isophote shapes are "disky" and "boxy". The galaxies with "boxy" isophotal shape are usually bright, fast rotators with strong X-ray emission if compared with the "boxy" ones (Bender et al. 1988). Kinematically, only disky ellipticals show a flattening due to their rotation whilst boxy galaxies are usually flattened by anisotropies.

The kinematic structure of ellipticals presents a wide range of behaviours, but it is a common feature that at their centre the observed velocity dispersion rises more rapidly than what predicted from the gravitational potential of the visible, baryonic matter. This is interpreted as a signal of the presence of a supermassive black hole (SMBH) in their centre (Galaxies formation and evolution, Mo, Van De Bosch, White). However, there are examples of galaxies with a flat sigma profile in the inner part which do host a SMBH (Mazzalay et al. 2016).

Elliptical galaxies are further classified in “power-law” or “core” based on the shape of their inner light profile (Kormendy & Bender 2009). The first class presents a power-law line profile up to the innermost observable radii, whilst the second shows a flattening in the inner parts. These populations can be distinguished from their kinematical structural proprieties (Cappellari 2016) that usually can be related to their different formation scenarios. Fast-rotator ETGs start as star-forming disks and evolve through a channel dominated by gas accretion, bulge growth, and quenching, whereas slow rotators assemble near the centers of massive halos via intense star formation at high redshift and remain as such for the rest of their evolution via a channel dominated by gas poor mergers.

Elliptical galaxies show very tight scaling relations, which connect kinematic and photometric proprieties and defined the so-called Fundamental plane, defined by:

$$\log R_e = a \log \sigma_0 + b \log \langle I_e \rangle + constant \tag{1.2}$$

where σ_0 is the velocity dispersion and a and b are constants that have been estimated for each photometric band. It is interesting to notice the small scatter around this relation shown by observations. In Figure 1.2 the plane is represented fitting a sample of almost 9000 galaxies. Here is possible to observe on the axis R_e, σ_0 and $\langle I_e \rangle$, from the three projections of this plane along these axis derives three important scaling relations that connects these quantities two by two.

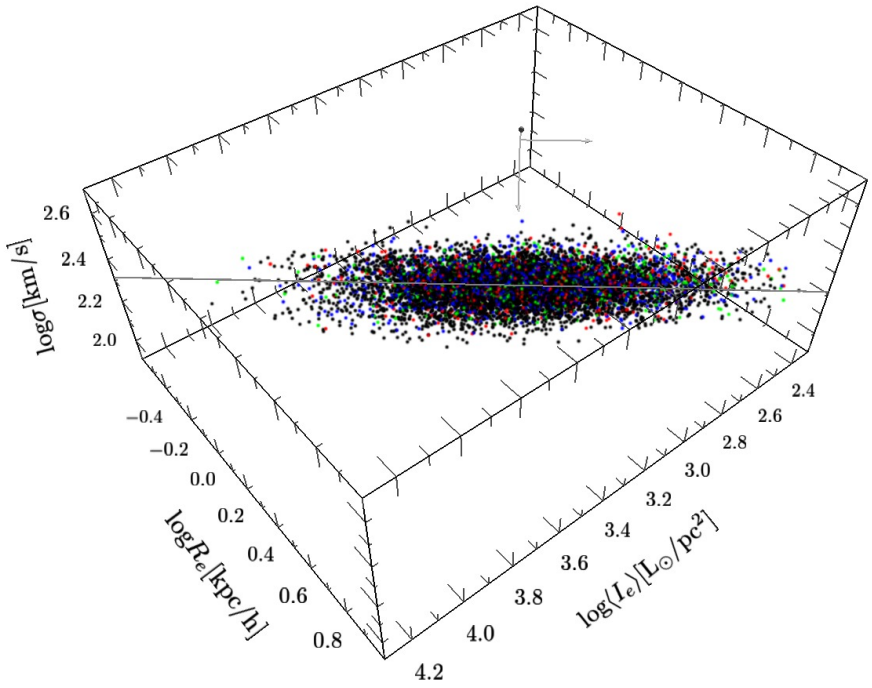

Figure 1.2: 3D visualisation of the 6dFGS J band Fundamental Plane with individual galaxies colour-coded by the richness of the group environment they inhabit: 6495 field galaxies in black; 1248 galaxies in low-richness groups in blue; 546 galaxies in medium-richness groups in green; and 612 galaxies in high-richness groups in red (these richness classes are defined in Magoulas et al. (2012)). The best-fitting plane (in grey) for the entire sample is shown for reference.

1.3 Spectral Energy Distribution

To study the proprieties of galaxies it is indeed necessary to combine many observables through structural, kinematical, chemical and spectro-photometrical analysis. To obtain a complete characterization of the stellar, dust, and gas content of galaxies, astronomers need observations at several different wavelengths. Unfortunately, not all of them are accessible from the ground as can bee seen in Figure1.3, which shows the atmospheric transmission at different wavelengths. For these reasons we often use a combination of ground and space based observatories, to get full access to the electromagnetic spectrum of astrophysical

sources. Each different wavelength implies different energy ranges, and so allow

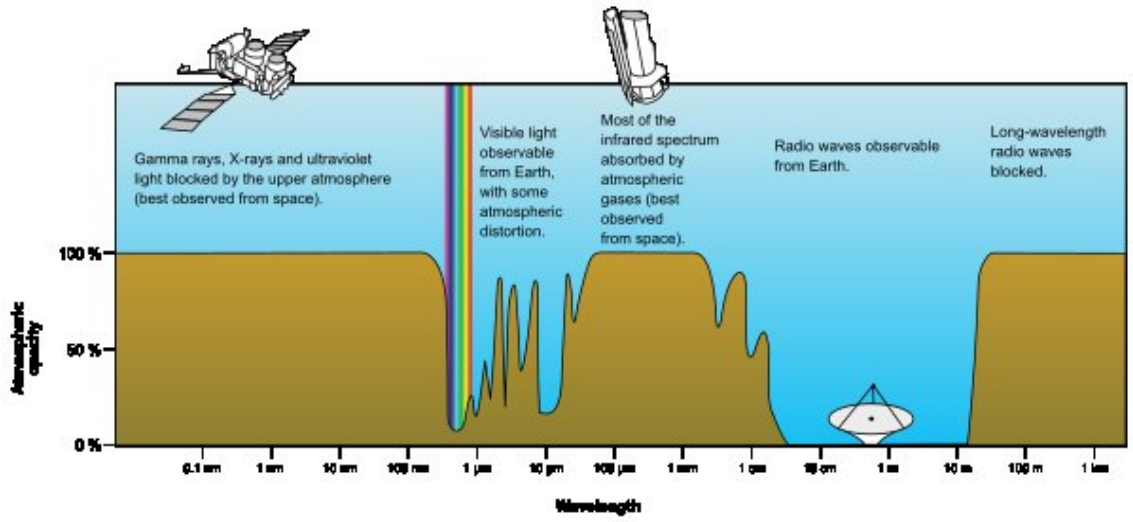

Figure 1.3: Atmospheric electromagnetic opacity [Credit:NASA (original); SVG by Mysid. Public Domain `https://commons.wikimedia.org/w/index.php?curid=5577513`]

us to study different physical processes. In X-ray is mainly possible to observe the thermal bremsstrahlung the accretion disk in binary systems and the hot gas ($10^6 - 10^8$K) that fills massive halos like clusters of galaxies. The stellar component of galaxies emit as a black-body in UV to NIR with different contributions depending on their ages. From UV to NIR is also possible to observe gas clouds ionized by hot and young stars (HII regions) through many emission and absorption lines from hydrogen and metals. These are the best diagnostics to study the process of recent star formation.

Moving further, in the medium- and far-infrared we can observe the spectral signatures from Polycyclic Aromatic Hydrocarbons (PAH), and constrain the hot and cold dust content of galaxies. Finally, in Radio band is possible to observe HII regions, emission and absorption line at 21cm from diffuse Interstellar Medium (ISM), and relativistic electron in the weak magnetic field (synchrotron radiation). Since here we are interested in studying the stellar content of passive, evolved galaxies with little or no gas and dust content; this work is based on optical and NIR observations.

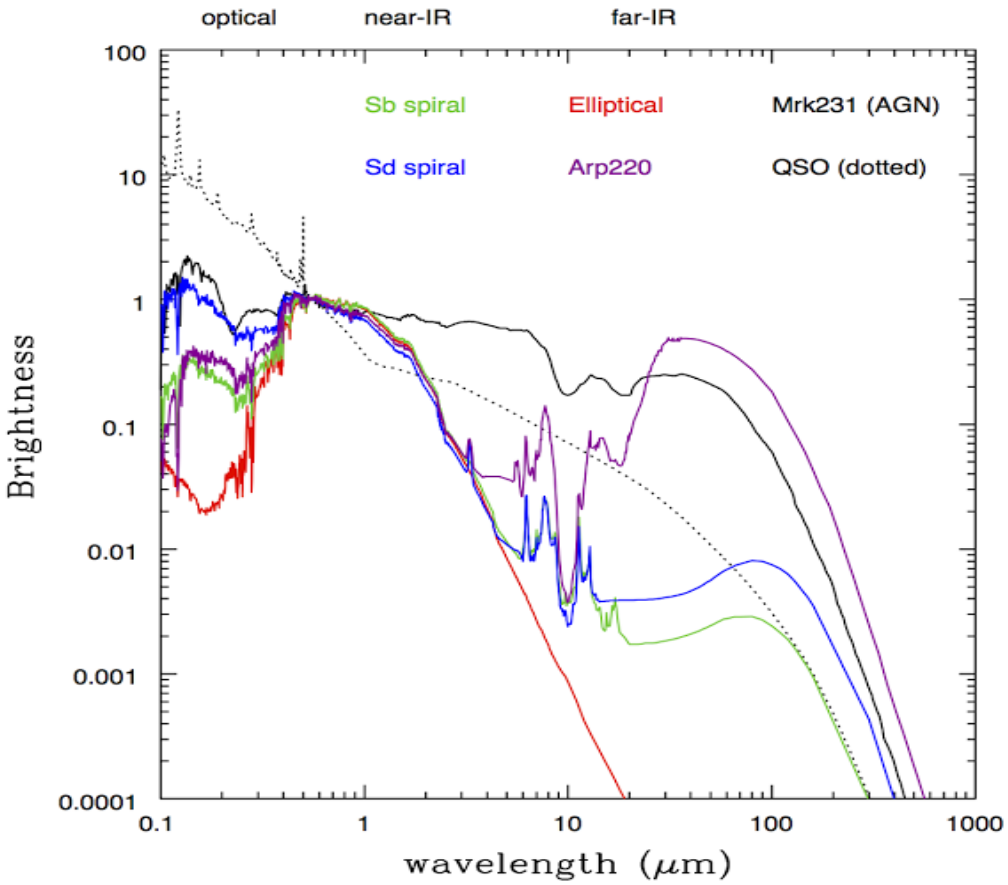

Figure 1.4: Spectral energy distributions for typical galaxies - an old elliptical galaxy (red), two types of spiral galaxies (Sb in green and Sd in blue), an AGN (Markarian 231, solid black), a QSO (dotted black), and a merging dust rich and star-bursting galaxy Arp 220. Template spectra are taken from Polletta et al. (2007)

The spectra of a galaxy is just the combination of its elements: stars, gas nebulae, and Active Galactic Nuclei (if present). In Figure 1.4 it is possible to see the Spectral Energy Distribution (SED) of different types of galaxies: in red an elliptical, in green a spiral Sb, in blue a spiral Sd, in solid black an AGN, in dotted black a Quasar stellar Object (QSO), and in purple a merging star-bursting galaxy. As can be seen in the figure, the flux produced by elliptical galaxies gives the lowest contribute to SED from 0.1 to 0.3μm (UV bands) and rapidly decreases above 11μm due to the absence of dust. Around 1μm the flux is similar for every object, while moving to larger wavelength the spirals show a flux amount in between

ellipticals and QSO.

It is possible to divide the spectra into two main components. The first feature is the continuum which gives the general shape of the spectra and its produced by stars, AGN emission and hot dust. Each of these processes obviously give the main contribute at different wavelengths. The others two important features are the absorption and the emission lines, the first ones are produced by the atmospheres of stars while the other ones derive from gas which has been photo-ionized by some kind of radiation. Since the smallest volume which can be singled out in the galaxy is a column with diameter of the order of the spatial resolution, is not usually possible to identify single stars and gas clouds, with the only exception of our own Galaxy and a few nearby dwarf satellites of the Milky Way.

The study of the features of a SED is thus crucial in understanding the physical processes involved in the observed object and its proprieties and evolution. For a correct interpretation of the UV-Optical-NIR spectra, it is necessary to know the mass and age distribution of the stellar populations since, for example, the most massive stars dominate the galaxy SED in flux (or brightness) in the UV-optical bands even thought they do not dominate the mass distribution.

<

1.4 The Initial Mass Function

The initial mass function $\psi(M)$ (IMF) describes the distribution of initial masses for a coeval population of stars, generally called a single stellar population (SSP). The IMF is defined as the number of stars in the interval $(M, M + dM)$, with limits determined by the hydrogen burning limit of $0.08 M_{\odot}$ up to an upper limit of $100 - 120 M_{\odot}$:

$$\psi(M) \propto M^{-x} \tag{1.3}$$

Where x defines its parametrization. Like it can be seen in Figure1.5 there are some different interpretations.

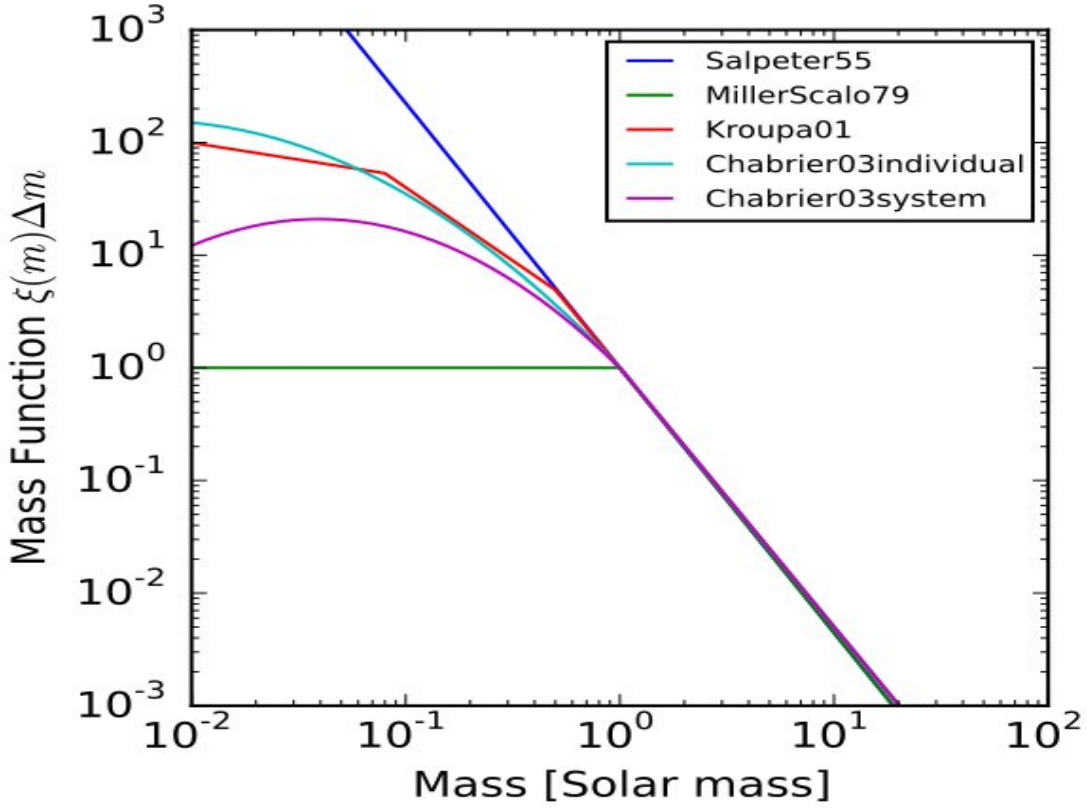

Figure 1.5: IMF Salpeter, Chabrier, Kroupa and Miller-Scalo parametrization [Credits: By Johannes Buchner - Own work, CC BY-SA 4.0, `https://commons.wikimedia.org/w/index.php?curid=44779435`]

The first formulation was made by Salpeter (in 1955) that found a value of $x = 2.35$. This formulation does not take into account stars with mass lower than $1M_{\odot}$, so later on Miller and Miller-Scalo (1979) extended this parametrization with a value of $x \approx 0$ for these lower masses. In 2001, Kroupa et al. suggested a revisited value of $x = 1.3$ between $0.08 - 0.5M_{\odot}$ and $x = 2.3$ above $0.5M_{\odot}$, which give a different ratio of high to low mass stars. More recently, Chabrier suggested a different interpretation for individual stars and for stellar systems, shown in Figure1.5.

The assumptions on the shape of the IMF affect the derivation of a large number of astrophysical proprieties such as the galaxy formation history, the mass-to-light ratio and therefore the stellar mass measurements. Despite this central role in many areas of astrophysics, a complete physical theory explaining the observed shape of the IMF is still missing. The IMF has been for long consid-

ered universal (invariant in space and time), because within the Milky Way there are no strong evidences of variations. However, theoretical studies do expect a variation (Conroy & van Dokkum 2012), and the debate about the main physical variables controlling it and their complex interplay is very open. Nonetheless, in massive early-type galaxies several studies (Cappellari 2012; Conroy & van Dokkum 2012; Thomas et al. 2011) found that the IMF shape changes as a function of stellar velocity dispersion or stellar mass with increasingly large number of low mass stars in galaxies with the highest sigma, even larger than the expectations from a Salpeter IMF (Conroy et al. 2013). Recently, Thomas et al. (2015) constrained the IMF in 9 massive elliptical galaxies using dynamical modeling to constrain the mass-to-light ratio. These results could be explained with a IMF which changes within the population of massive elliptical galaxies characterized by different light profiles in their inner parts, or by a systematic variations in the distribution of dark matter among massive power-law ellipticals.

1.5 This thesis

This thesis builds upon the results of Thomas et al. (2015) and aims at constraining the dependence of the IMF in local elliptical galaxies studying their stellar populations with the Lick (Worthey & Ottaviani 1997) indices technique adapted to the NIR bands. The sample includes 2 galaxies NGC7619 and NGC1332, presenting either "core" or "power-law" photometric profiles. To achieve strong constraints on the IMF we use integral field spectroscopic observations from the second generation KMOS and MUSE instruments at the ESO Very Large Telescope. These instruments provide us with data in the 0.8 to 1.1μm wavelength range where the galaxy spectra are rich of IMF sensitive features. My analysis makes mainly use of the CaI, NaI and FeH Wing Ford Band. The calcium Triplet is useful to measure the velocity dispersion while the other two features are sensitive to the IMF.

In chapter 2 I present the sample and the instruments used for the observations, in chapter 3 is shown the data reduction process for KMOS and MUSE , in chapter 4 I proceed with the data analysis thought the measurement of their kinematical proprieties and their Lick indices, and comparing my results with several populations models, lastly in chapter 5 I present the summary and conclusions of this work.

Chapter 2

Sources & Instruments

2.1 Sources

The sample chosen for this work consists of two early-type galaxies: NGC 7619 and NGC 1332. The first is an elliptical core galaxy (E), located in the Local Group, and it appears on the sky in the Perseus constellation. Its equatorial coordinates are RA=23h20m14.532s DEC=+08d12m22.48s (J2000). Its optical image is shown in Figure 2.1. NGC 7619 redshift is $z = 0.012549 \pm 0.000017$ (Trager et al. 2000) and its distance is 53.780 Mpc. It has an apparent diameter of 2.5 arcmin along the major axis and 2.3 arcmin along the minor one, and is characterized by an high velocity dispersion ($\sigma \sim 300\, km/s$, Wegner et al. 2003). The absolute visual magnitude is $M_V \approx -22.94$ (Lauer et al. 2007). This galaxy has also been found in tidal interaction with NGC 7626 (Rembold et al. 2002), a lower mass neighbor. The variety of dynamic and spectroscopic studies performed so far indicates that NGC 7619 is an ideal target for studies of stellar populations in elliptical galaxies and of the stellar IMF.

The second galaxy analyzed in this work, NGC 1332, is a massive elliptical galaxy morphologically classified as S0, located at RA=03h26m17.252s, DEC=-21d20m06.78s in equatorial coordinates (J2000). It appears on the sky in the Eridanus constellation. It is a normal lenticular galaxy with a close to edge-on orientation. Its redshift is $z = 0.005084 \pm 0.000033$ (de Vaucouleurs et al. 1991), corresponding to a metric distance of 22.936 Mpc. It has a major axis diameter of 4.7 $arcmin$ and a minor diameter of 1.4 $arcmin$. It presents a high velocity dispersion ($\sigma \sim 320\, km/s$, Rusli et al. 2011) and recently (Barth et al. 2016) performed gas kinematics studies and measured for the central super massive black hole (SMBH) a mass of $\sim 4 - 8 \cdot 10^8\, M_\odot$. The nature of this galaxy and its presence in several dynamical models such as Thomas et al. (2014) make of it a perfect observables for this work.

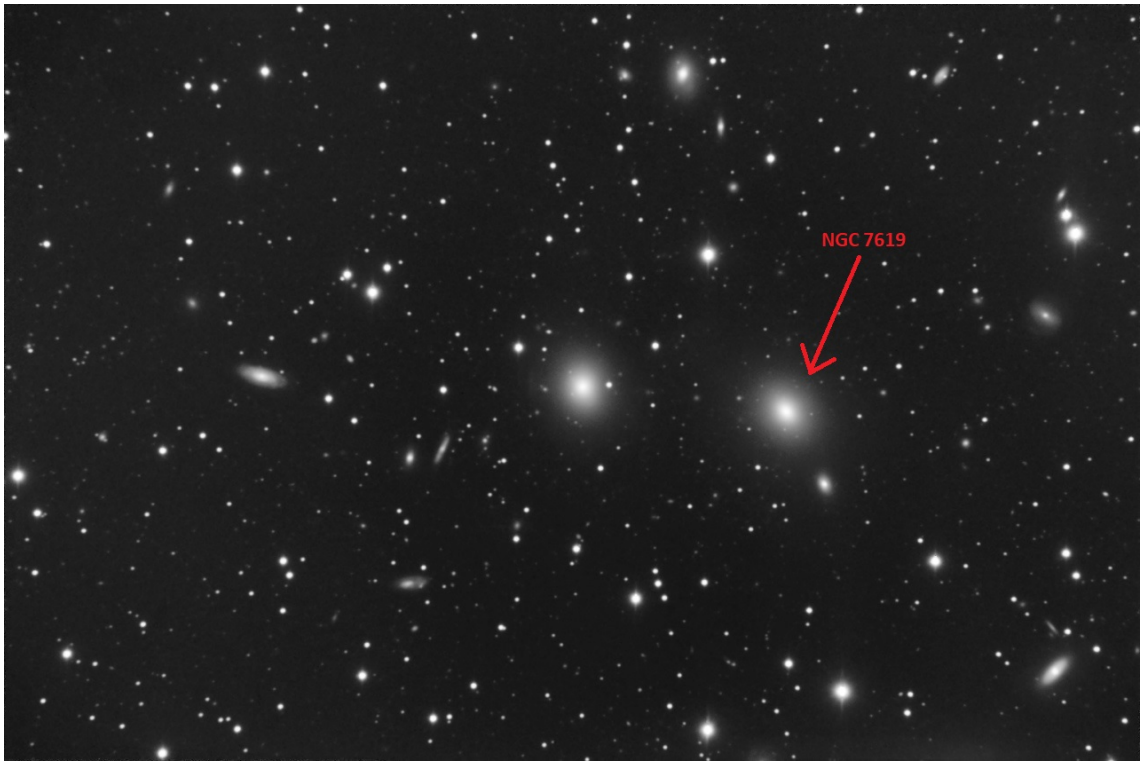

Figure 2.1: An optical image of a group of galaxies in the direction of the Perseus constellation. NGC7619 is highlighted with a red arrow. [Credits: http://www.jburnell.com/NGC7619.html]

2.2 Instruments

For the purposes of this work, we need deep, intermediate resolution spectra covering the inner regions of the target galaxies. To perform this study, Integral Field Spectroscopy (IFS) represents an ideal choice. We therefore chose two Integral Field Units instruments, exploit data from two integral field unit instruments mounted at the Very large telescope (VLT) facility operated by the European southern observatory on Cerro Paranal, Chile. The VLT consists of an array of four 8.2-meter telescopes which can work independently or in combined mode, allowing for interferometric observations. Each telescope is a Ritchey-Chretien configuration. This scheme employs a hyperbolic primary mirror and a hyperbolic secondary one, and is designed to eliminate off-axis optical errors (coma). The mounting is alt-azimuthal, since each telescope has three main focii: two Nasmyth platforms on each side of the altitude axis host large and complex instruments, while the Cassegrain focus below the primary mirror cell hosts lighter

instruments.

Before describing in details the two instruments we give an overview of integral field techniques. Figure 2.2 shows the schematic picture of the signal flow from the observation to the scientific data in an IFU. First, the light from the source gets sliced by means of optical devices and it is re-arranged onto a long slit. Then a dispersing element separates the light along the wavelength axis, and the spectra are saved onto the camera detectors. Lastly all the spectra are arranged into a datacube which contains the entire 2D field of view plus a third dimension that represents the spectroscopic axis. With this technique it is therefore possible to obtain a spectrum for each 2D pixel observed.

Thanks to this technology to cover an object two-dimensionally is no longer necessary to perform several exposures with altered slit positions.

2.2.1 MUSE

One of the instruments used for my thesis is the Multi Unit Spectroscopic Explorer (MUSE) shown in Figure 2.3, which is mounted on the VLT UT4 telescope. As already mentioned, MUSE is an Integral Field Spectrograph, equipped with 24 Integral Field Units (IFU), with two observing modes: Narrow Field and Wide Field. Currently only the Wide field mode is offered to the scientific community. In the Wide Field Mode (WFM), MUSE splits the field of 1 $arcmin^2$ in the 24 IFUs. Then the signal goes through a slicer that splits the light in further 48 parts called mini slits. A this point the grating of the spectrograph disperses each mini slit in the perpendicular direction and image them onto the CCD.

From Figure 2.4 one can see the trend of the spectral resolution of MUSE growing with the wavelength. The spectrograph achieves spectral resolutions from 1750 at 465 nm to 3750 at 930 nm. Two possible modes are available when observing in Wide Field, the nominal and extended one. Because the gratings work in second order (to achieve a moderately high spectral resolution), the light bluer than 480nm is projected onto the detectors out of focus above 800nm, producing artifacts that degrade the quality of the spectra. Whenever it is not necessary to observe the spectral range 465-480nm (extended mode), a cut off filter is introduced in the optical path, limiting the spectrum to wavelengths above 480nm but removing the effects of second order contamination (Nominal mode). In nominal mode, as can be seen in Figure 2.5, the signal drops to zero at 480 nm, while in the extended one can reach 465 nm.

2.2.2 KMOS

The second instrument used in my thesis is the K-band Multi Object Spectrograph, KMOS. Active from 2012, the instrument is mounted on the UT1 telescope at the VLT. KMOS has 24 pick-off arms that can be positioned independently. The arms are arranged in two layers to reduce arm collisions and the arms can patrol an area of 7.2 arcmin in diameter. Each arm has an IFU with a squared field of view of $2.8 \times 2.8\, arcsec^2$. The light collected from each IFUs goes into a slicer that divides the beam into 14 identical parts, with 14 spatial pixels along each slice. The signal from the IFUs is then dispersed by three cryogenic grating spectrometers which generate 14×14 spectra.

KMOS has five grating options, for five spectral bands: IZ, YZ, H, K, HK. For each spectral band there is a different resolving power and each of the three spectrograph is characterized by a slightly different wavelength coverage. For example, in IZ the spectral resolving power in the band center is 3406 and the wavelength coverage of the spectrograph B is $0.779 - 1.094\, \mu m$.

KMOS allows three different observation modes: nod-to-sky, stare and mosaic. The first two differ in how the background signal is detected. While in nod-to-sky each arm switch from the targeted object to the signal free sky, in stare mode there are dedicated arms pointing the sky background. On the other hand, the mosaic mode allows for the observation of contiguous fields on the sky (Mosaic) instead of multiple isolated targets. In this mode it is possible to cover a rectangular area of the sky in two possible configurations, the first involving all 24 IFUs arranged in a 6×4 array. In the second, 3 subgroups of 8 IFUs each are arranged in a 4×2 arrays. In order to avoid gaps, all the IFUs are evenly spaced from each other by a distance slightly smaller than an integer multiple of the IFU size.

Figure 2.7 shows the system efficiency of KMOS in the IZ band as function of the wavelength, calculated using the web tool "KMOS exposure time calculator" developed by ESO. It is possible to see that the system efficiency grows with the wavelength and drops when it reaches the coverage limit for this band, at $1.094\, \mu m$. Lower values of system efficiency mean that only a small percentage of the signal from the beam is actually been detected. In order to correct this issue longer exposure times are needed.

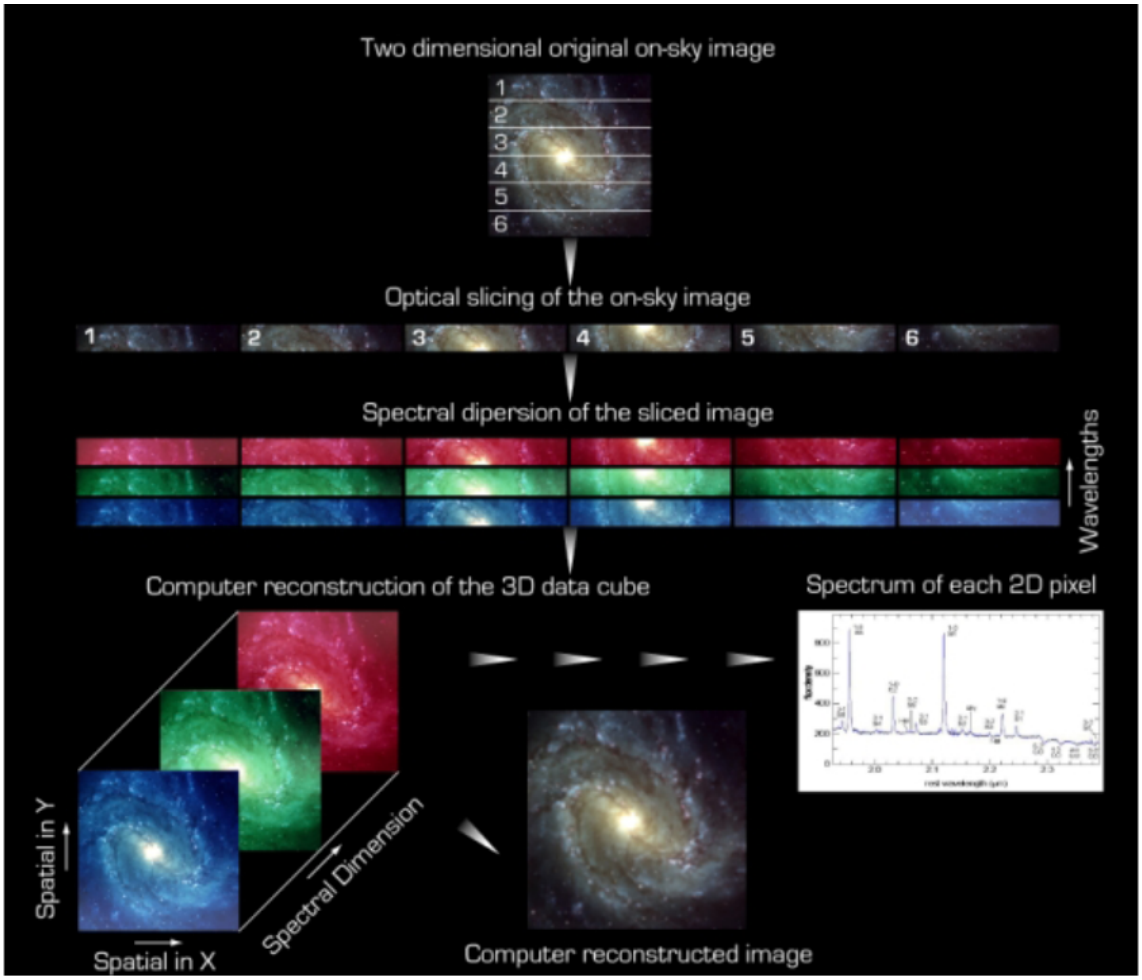

Figure 2.2: Integral Field Spectroscopy analysis procedure [Credit: https://www.eso.org/sci/facilities/paranal/instruments/kmos/doc/VLT-MAN-KMO-146603-001_P100.pdf]

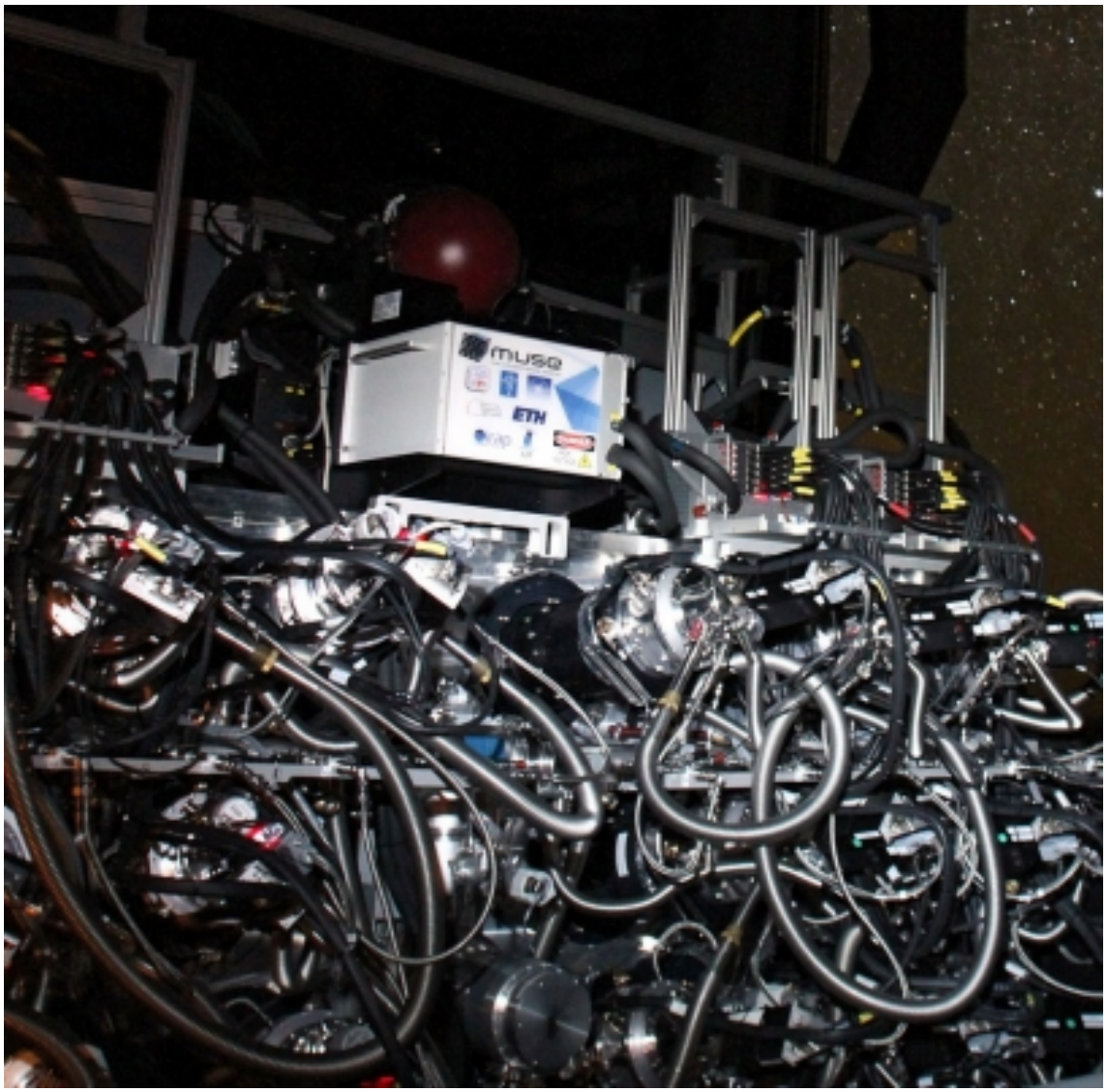

Figure 2.3: MUSE [Credit: http://www.eso.org/sci/publications/announcements/sciann14012.h

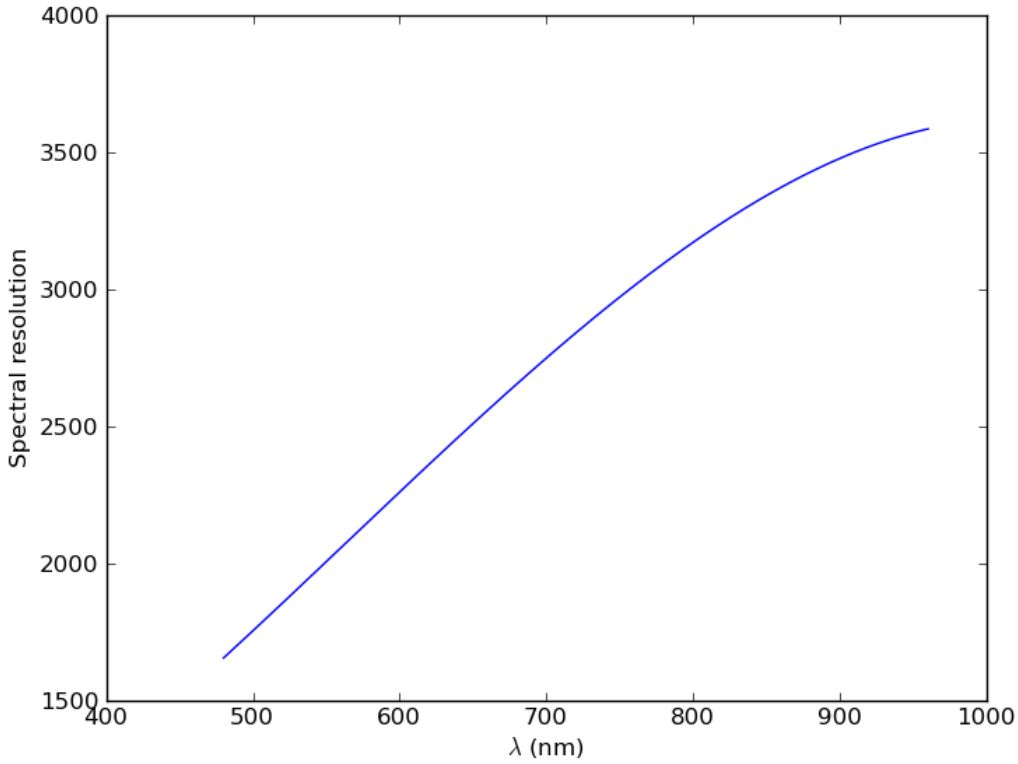

Figure 2.4: Muse spectral resolution [Credit: `https://www.eso.org/sci/facilities/paranal/instruments/muse/doc/ESO-261650_7_MUSE_User_Manual.pdf`]

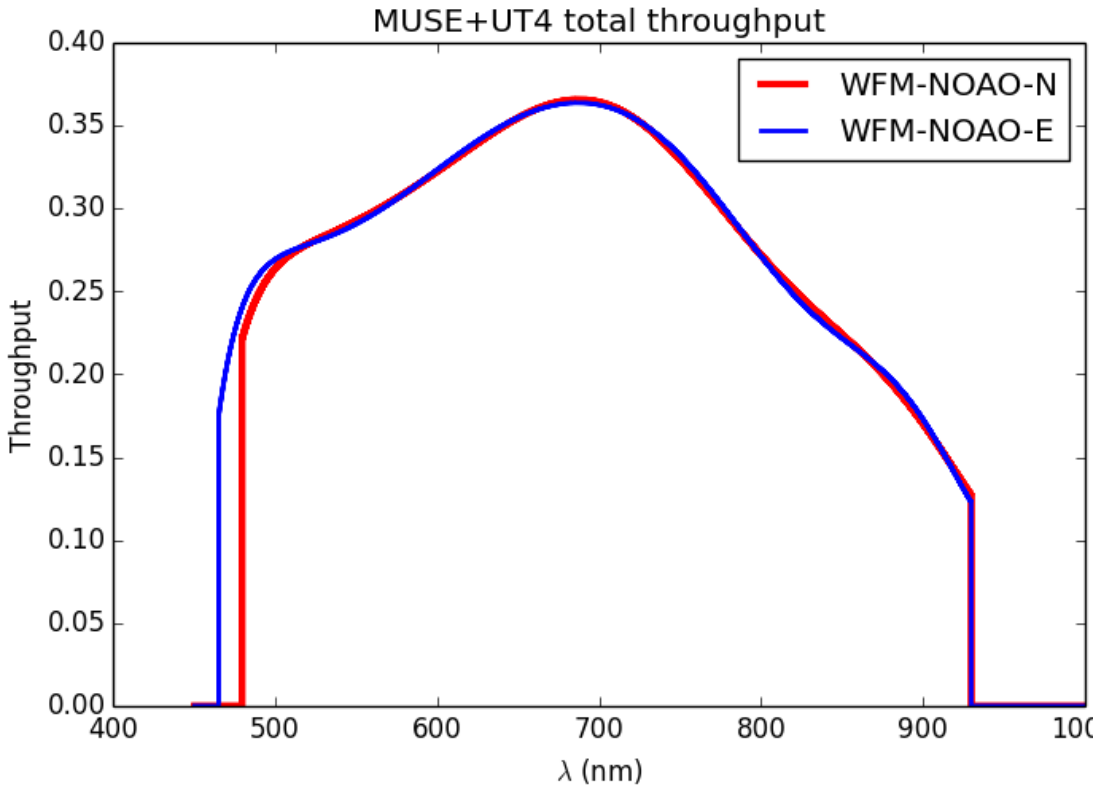

Figure 2.5: MUSE Throughput of Nominal and Extended mode [Credit: https://www.eso.org/sci/facilities/paranal/instruments/muse/doc/ESO-261650_7_MUSE_User_Manual.pdf]

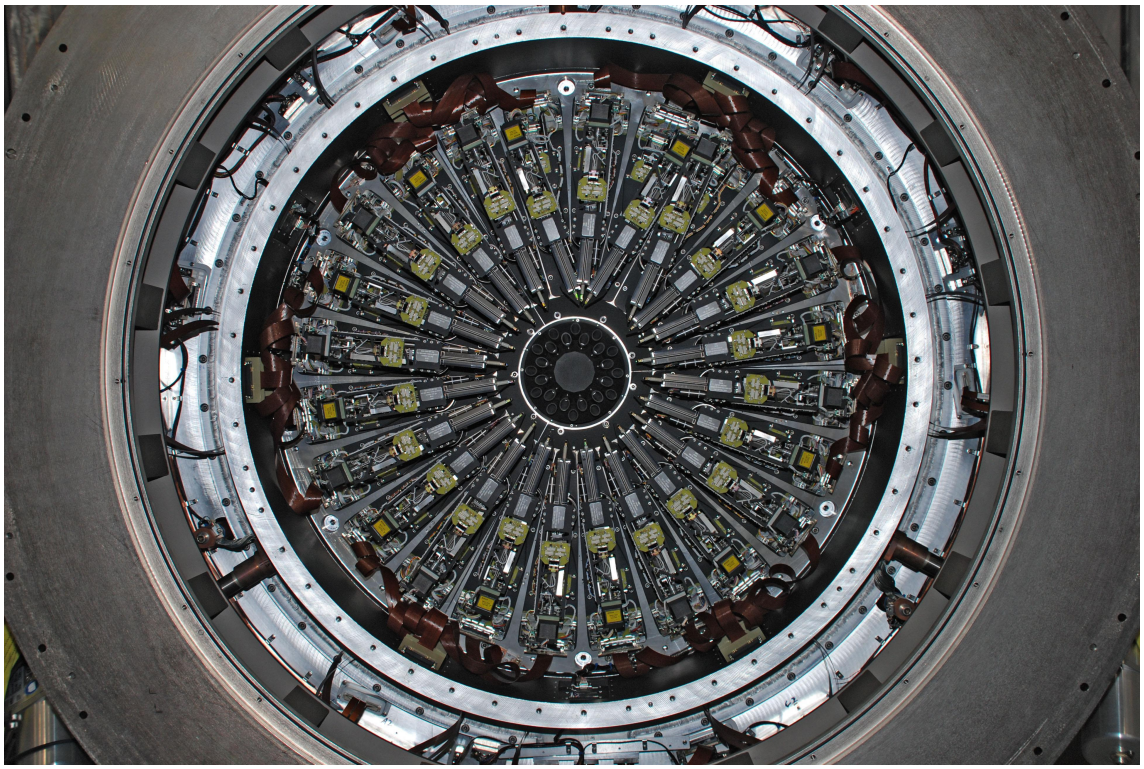

Figure 2.6: The full 24 pick-off arms in the front end of the KMOS cryostat. [Credits: https://www.eso.org/sci/facilities/paranal/instruments/kmos.html]

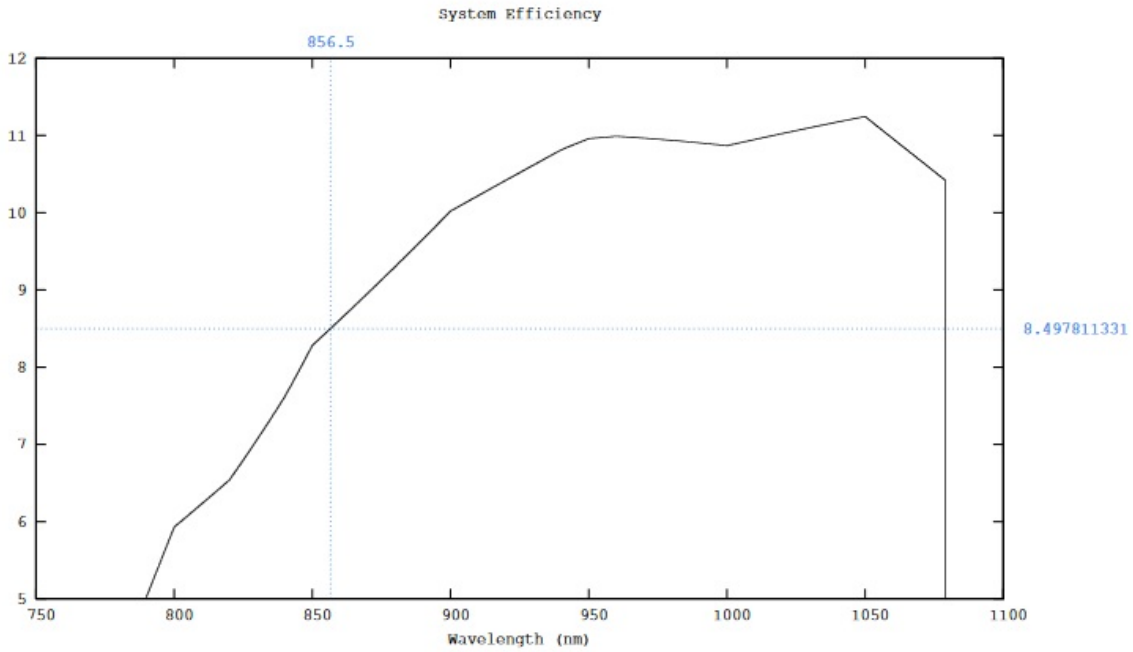

Figure 2.7: KMOS throughput in IZ band [Credits:https://www.eso.org/observing/etc/bin/simu/kmos]

Chapter 3

Data Reduction

To obtain science grade data, from raw exposures, a reduction and calibration process is essential. Both for the KMOS and MUSE instruments, a data reduction pipeline is made available by ESO and the instrument teams. One way to run the instrument pipeline is via the ESO Recipe Exection Tool (ESOREX). In this software, the data are processed through recipes. Every recipe operates a different step of the reduction, allowing the user to modify the recipe options to suit various needs. Every recipes fed with a Set of Frames (SOF) file: a text file containing the path of the input and calibration files needed to execute that recipe .

In this work, to reduce KMOS data, I used the Software Package for Astronomical Reductions with KMOS (SPARK Davies et al. 2013), which, as described above, can be run within ESOREX. To reduce the raw data collected by the telescope from observations, these two pipelines for KMOS and MUSE share the same physical approach, but with different implementations. The basic steps, common also to most of the optical/near-infrared spectroscopic observations, are: dark, flat field, wavelength, illumination, and flux calibration.

Since the dark current (constant response exhibited by a receptor of radiation during periods when it is not actively being irradiated) is negligible both in KMOS and MUSE; the dark calibration in KMOS is only needed to detect a bad pixel map, while in MUSE is usually skipped. The dark calibration is performed with the telescope's shutter closed, but with all the electronics activated. The bias is then an additional signal, that has to be subtracted from the bi-dimensional spectrum. The next necessary step is the flat field calibration. This procedure is needed to correct pixel sensitivity variations. It is performed by taking daily several exposures of the internal continuum lamp with constant intensity. Usually, after acquiring several flat field exposures, the image is divided by the normalized value. The following step needed is the wavelength calibration, that must be checked once per day. In this process, some frames of the arc lamp (Ar,Kr) are taken, then the location of these reference emission lines on the detector is

used by the data reduction software to derive a wavelength solution via a dispersion relation. This relation associates each pixel position to the corresponding wavelength. At this point a sky-flat calibration is necessary to correct the illumination of the sky. This correction usually delivers an illumination correction good to a few percent level . This is done by taking some exposures during twilight. Another, crucial step consists of removing the telluric features in the spectrum, which are produced by the Earth's atmosphere. Since the latter is highly variable, telluric lines change as well rapidly, and they do not scale linearly with the air mass above the telescope. In order to correct for this issue, observations of standard stars, with known spectra, are needed. These must be done with the same instrumental setup and as close in time as possible to the target observation. The observation of standard stars is also essential for the flux calibrations: convert the CCD's counting in a flux measure. To do that, stars need to have well known spectra usually from the HST CALSPEC library or from knowledge of their blackbody emission and temperature. The known spectrum is compared to the observed spectrum to obtain the response function of the instrument plus grating setting (instrument throughput as a function of wavelength), and the zero point of the observation. The latter is the scaling factor to convert detector counts into physical units (either $W/m^2/A$ or $erg/cm^2/s/A$).

The exact procedure to be followed to obtain scientific data from the observations through the pipelines is explained in the following sections, for each of the two instruments.

3.1 MUSE

The observations have been performed for both instruments with two exposures of 900 seconds and 300 seconds on the sky, on the night of 18-09-2015 for NGC 6719 and on the night of 07-09-2015 for NGC 13332.

Selection of the input files Running the MUSE pipeline recipes using EsoRex requires that the user prepares the set-of-frames file. To be able to do this one has to find the correct input files for each recipe and assigns the correct frame tag and one has to find calibration file which were taken with a matching instrument configuration. The type of a MUSE raw data files is fully determined by a unique combination of the header keywords *CATG*,*TYPE*, and *TECH*. The last step in creating set-of-frames files as input for the MUSE recipes is to find the appropriate calibrations both, the static and the daily calibrations. This means that one has to select calibrations which originate from the same (or compatible) instrument configuration. To find a calibrations with a matching instrument setup

one can use one of the header keywords depending whether the whole instrument configuration should match (or only the field mode), *INS.MODE*: provide information on the field mode (wide or narrow field) and whether the AO was used, and, whether the nominal or the extended wavelength range . The other keyword is *INS.OPTI2.NAME*, that contains only the setup of the field mode. It may be used in cases where the other parameters of the instrument setup do not matter. Finally, if one obtains calibrations as part of an archive request from the ESO archive, then the ESO archive took already care that they match the raw data of the request. Thus, there may be no need to redo the data association.

Bias subtraction During the first processing step, the raw bias frames are combined into a master bias frame using the *muse_bias* recipe. The created master bias will then be used in the subsequent reduction steps. First the location and the raw frame tag of at least 3 raw bias frames is put into the set-of-frames. Without the option "–merge" the recipe produce 24 FITS files with 3 FITS extensions each, where the IFU from which it has been created is indicated by the 2 digit sequence number at the end of the file name. The dark correction in MUSE is optional and generally not necessary, because the dark current of the MUSE CCDs is very small and the bias calibration already take care of the main calibration of the detectors.

Flat fielding The flat field correction is been done through the *muse_flat* command. The set-of-frames must contain at least 3 raw flat field frames and the master bias frame. The products of this EsoRex command are the master flat frame and the trace tables, each of them stored as single FITS files containing the master flat field and the tracing solution for all IFUs respectively. Similarly to other IFU instruments, the MUSE pipeline uses these calibrations to calibrate the position of the field of view onto the 24 CCDs, to derive an illumination and throughput correction for the different CCDs.

Wavelenght calibration In the next processing step the wavelength solution for each IFU is created using the recipe *muse_wavecal*. To create the dispersion solution the recipe needs at least three raw arc-lamp frame as input, which corresponds to one raw frame for each available arc-lamp. It is possible to use more than one of these sets as input.These sets of three arc-lamp frames are created by the MUSE calibration template and therefore a complete set should always be available. For illumination correction, twilight flats are part of the regular calibrations taken for MUSE. In this processing step the raw sky-flat frames are combined into a three-dimensional illumination correction using the recipe *muse_twilight* In addition, the created twilight-cube carries the integrated flux

value on to the further processing steps, as an estimate of the relative throughput of the IFUs. The recipe needs as input at least 3 raw sky-flat frames, the master bias frame, the master flat field, the trace table, the wavelength solution and the geometry table. The primary product of this processing step is the twilight cube, which is a data cube of the smoothed twilight sky. As an additional product the data cube created from the combined twilight images is available: the data cube of the twilight sky before the smoothing is applied. The recipe works on the data of all 24 IFUs simultaneously. It should be noted that, even after applying the illumination correction from the flat fielding and the twilight cubes steps, an inhomogeneity of a few percent level remains across the field of view. This is likely related to rapid temporal variations in the throughput due to variations in temperature, or in the detector electronics. This effect, however, is minimized by combining multiple exposures taken at different rotator angles.

Cube reconstruction and sky subtraction At this point all necessary calibrations have been created to remove the instrument signature from the on-sky exposures using the pre-processing recipe *muse_scibasic*. This also converts the observations to the pixel table format which is the input format for the post-processing recipes. During this conversion sky lines are used to correct for offsets in the wavelength solution and, optionally, the data is corrected for the relative illumination of the slices for individual IFUs.

At this point it is possible to run the final processing leading to the creation of the final datacubes for the science observations using *muse_scipost*. The recipes apply the previously created on-sky calibrations, as such, the input set-of-frames will contain the 24 pre-processed pixel tables of the exposure of the science target, the estimated fluxes of the sky lines, the response curve, the telluric correction, the extinction table, the astrometric calibration, and the list of filter transmission curves. By default the recipe performs a model based sky subtraction, i.e. initially a model of the sky lines and the sky continuum are computed using the darkest regions in the field-of view, and then these models are subtracted from the data. To refine the sky subtraction from the pipeline it is been used the tool Zurich Atmosphere Purge(ZAP) The method uses PCA to isolate the residual sky subtraction features and remove them from the observed datacube. Since ZAP is not dependent on perfect flatfielding of the data in a MUSE exposure, better results are obtained. Finally, the datacubes gets combined in a final cube with spatial sampling 0.2" and spectral sampling 1.25 Å.

3.2 KMOS

The observations have been performed on the 2017-09-10 for NGC 7619 and on the 2013-11-01 for NGC 1332. The data have been collected with the mosaic mode, centered respectively on the IFU16 for NGC 7619 and on the IFU14 for NGC1332. The pipeline for used for KMOS data reduction has been SPARK as mentioned above.

Dark calibration The dark calibration in KMOS is performed taking exposures of 60 seconds. Flat frames are taken in all the five bands and at six fixed angles with respect to the north of the Nasmyth focus (0,60,120,180,240,300). This ensures that the effects of gravity on the optical and mechanical parts of the instrument can be accurately corrected.

Flat fielding and wavelength calibration The flat exposures are used to identify the position of the slit of each IFU onto the detectors and therefore to create a map of the spatial position on the sky of each detector pixel (XCAL and YCAL). This will be used with the wavelength calibration to reconstruct the detector images into 3-D datacubes. The wavelength calibration is executed with Ar and Ne lamps. These exposures are taken at different angles and for all the bands observed during each night, and are used to produce a map of the wavelength of each pixel on the detectors (LCAL). From the arc exposures it is also possible to obtain an estimate of the spectral resolution of each IFU. To do so, first we reconstruct the arc exposure using the geometry calibrations (XCAL, YCAL, LCAL), then we collapse each IFU into a single spectrum using a median combine. Lastly we measure the width of the brightest and most isolated skylines using an IDL code (*kmo_instrres*) developed by M.Fossati for the KMOS^{3D} pipeline. In Figure 3.1 I show the resolution obtained in the IZ band for the central IFU(16) of the mosaic of NGC7619. The black dots represent the resolution derived from individual arc lines across the wavelength range, while the brown solid line is a 4th order polynomial fit of the points.

Telluric correction To remove the telluric absorption features of the Earth's atmosphere from science spectra, I have included in the reduction sequence, a step based on the Molecfit software (Smette et al. 2015) to fit the telluric absorptions directly in the target spectrum. This code produces an atmospheric model tuned to the observed weather conditions to correct the spectra with high fidelity. The molecules involved in this process are: H_2O, CO_2, O_3, N_2O, CO, CH_4 and O_2. To join the telluric absorption correction with the flux calibration, I first derived a response function from a calibration star (observed during the same night of the

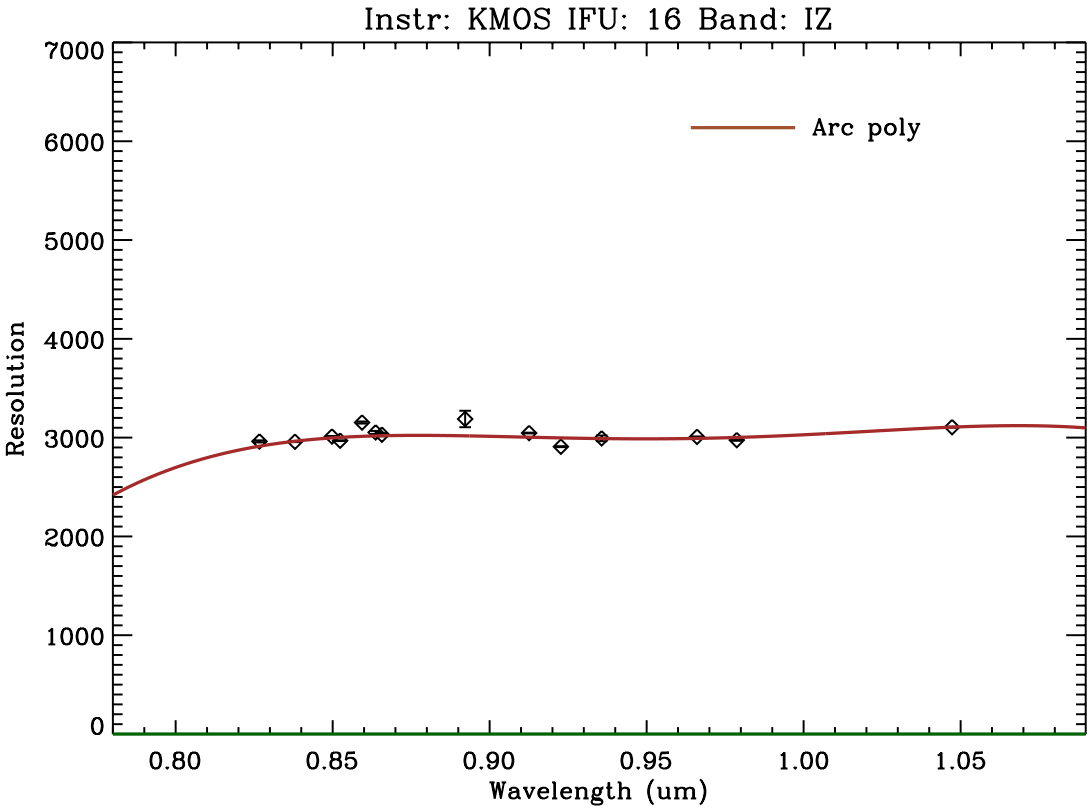

Figure 3.1: KMOS resolution in IZ for the central IFU 16

data) observed in the IFU 4, 12 and 18. The difference between the response of the IFU12 to the central IFU in my galaxies (IFU16 for NGC 7619, and the IFU14 for NGC 1332) has been tested to be a small factor, using an observation of a calibration star in all the 24 IFU (collected in 2014), showing an average difference of $\lesssim$ 5% negligible for our purposes. Then, it is been possible to apply confidently the output absorption model from molecfit to the response function derived form the IFU 12 to my central IFUs. We choose the IFU12 since is the closest to our observation IFU and it is in the same detector. This response function with the molecfit output has been then given as input in the pipeline as the optional telluric product in the *KMOS_SCI_RED* recipe.

Cube reconstruction The *KMOS_SCI_RED* recipe finally allow me to process the science frames applying the full set of processed calibrations. This workhorse recipe performs all the steps necessary to go from raw data to science cubes:

namely flat fielding, illumination correction, reconstruction of the 3-D datacubes using the geometry tables (XCAL, YCAL, LCAL), telluric correction, flux calibration, and subtraction of the sky background (continuum and air-glow emission lines). This recipe is also able to shift and combine the data into a final datacube, however, because data for the same object might be taken during different observing nights, we usually run the combine step separately.

I have used some specific options when running KMOS_SCI_RED. First of all, I used the *VELOCITY_OFFSET* option, to apply a constant velocity offset (in km/s) to the data during reconstruction to take into account for the Earth's orbital velocity. I also provide the code with a high-resolution and high signal to noise OH spectrum in IZ band (provided with the static calibrations of SPARK). This is used by the code to further refine the LCAL calibration for each individual exposure, to reach a higher quality flux calibration. This step is critical to obtain a better subtraction of the sky lines which is achieved in combination with the use of the *SKY_TWEAK* option. This advanced sky subtraction method enhances the OH removal, via flux scaling of the OH lines in the sky exposures which have a different flux from those in the science data due to the variation of the line fluxes during the night. I also forced the pipeline not to subtract the residual background *BACKGROUND= False*. This option is useful in case of compact (point-like) sources where some of the spectra are sampling the sky background. In case of extended galaxies this option would simply subtract the source from the datacube and therefore should not be used with our massive local elliptical. Instead I let the pipeline to subtract the sky continuum from the dedicated sky exposures using the TBSUB= True option. Lastly, I triggered the *NO_COMBINE* option, to perform this step separately.

Generation of combined cubes In the last step the individual exposures are shifted and then combined to achieve a higher signal to noise. I used the option *edge_nan* to set the single row or column of pixels at each border of the cube to be NaN. This minimizes unwanted border effects resulting from poor image quality at the edges of the slitlets, a known feature of KMOS data. The shifting option *METHOD= header* has also been activated, to compute the needed shift according to the WCS information stored in the header. I further call up the option *name* to combine the IFUs separately.

The steps described above allowed me to derive spectra, shown in Figure3.2 for NGC 7619 and in Figure 3.3 for NGC 1332, with a signal to noise ratio in the central IFU for NGC 7619 and for NGC 1332, where we reached $S/N \sim$100 and 80 respectively.

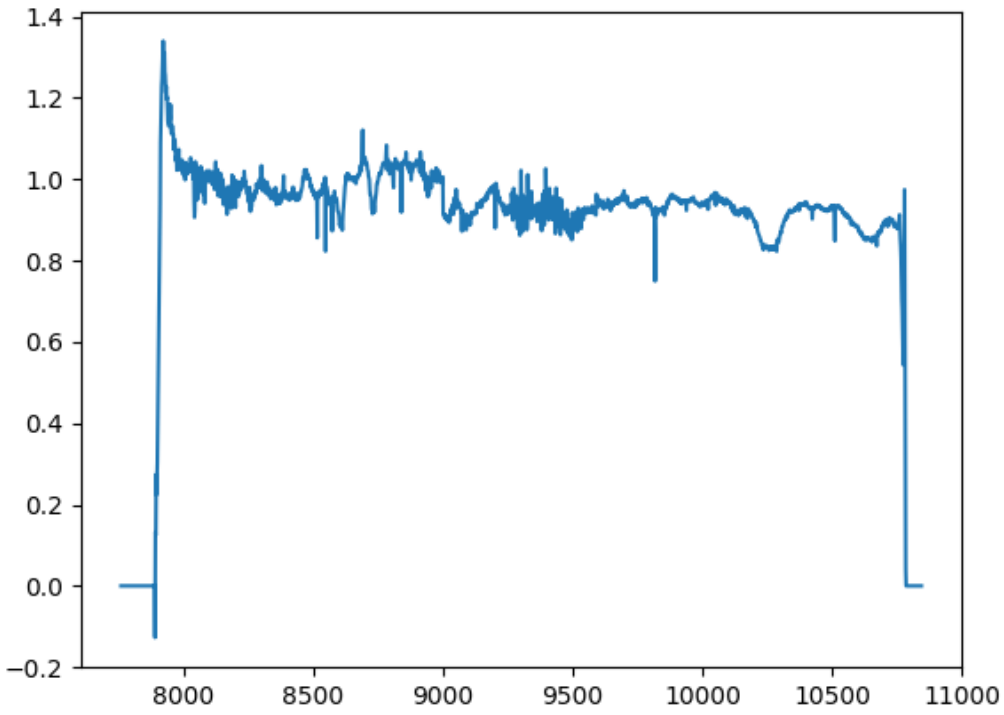

Figure 3.2: KMOS NGC7619 spectrum for the central IFU 16

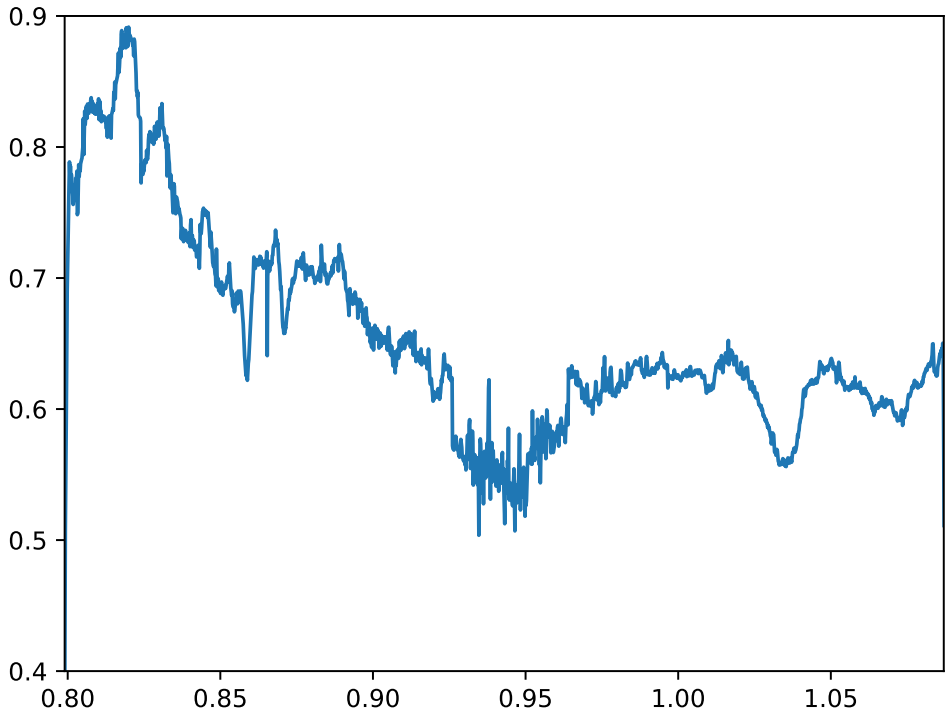

Figure 3.3: KMOS NGC1332 spectrum for the central IFU 14

Chapter 4

Data Analysis & Results

4.1 Kinematics

The study of the galaxy kinematics is a critical diagnostic to understand several astrophysical processes both involving the gas phases in and around galaxies or their stellar content, including but not limited to the star formation, the gas accretion during the galaxy assembly, the composition of a galaxy (stellar and dark matter content) and galaxies mass distributions and scaling relations. (see e.g. Cappellari et al. 2016 for a review.)

4.1.1 Physical Approach

The kinematical proprieties of early-type galaxies are derived from absorption lines in the spectrum. Typically, bright, boxy ellipticals are slow rotators, supported by anisotropic velocities, while fainter, disky elliptical have much higher velocities. Since ellipticals galaxies are generally pressure supported systems, the measurement of velocity dispersions is of paramount importance, this is indeed directly related to the dynamical total mass of elliptical galaxies by the equation:

$$M(< r) = \frac{3\sigma_0^2 r}{G} \tag{4.1}$$

where σ_0 is the observed velocity dispersion along the line of sight. This kinematical relation is thus one of the most important direct observational constraints for models of galaxy formation and evolution, because of its tight connection to the dark matter content of elliptical galaxies. To determine the velocity dispersion along the line of sight of elliptical galaxies we measure the width of absorption lines in their optical spectra. Since the line profiles are not simple Gaussian functions, an accurate measurement of sigma is achieved by fitting the galaxy spectra

with stellar templates, convolved with a broadening due to random motions of the stars in the galaxy. Since is not possible to derive the orbits of stars in three dimensions, we can only measure radial velocities and velocity dispersions along the line of sight.

The radial velocity is measured from the position of the lines which is shifted with respect to the laboratory known values due to the Doppler effect. For small deviations from a reference velocity we can write:

$$v \approx c\frac{\Delta\lambda}{\lambda_{\text{emit}}} \approx c\,\Delta \ln \lambda. \tag{4.2}$$

Because the smallest volume which can be singled out in the galaxy is a column with diameter of the order of the spatial resolution (which is of the order of 1-2 arcsec in our MUSE/KMOS data), we only obtain the line-of-sight velocity distribution (LOSVD, $L(y)$) within these apertures. In more details, the template is a suitable combination of stellar spectra of different spectral types which are then convolved with a parametric function which represents the line of sight velocity dispersion. This function is a Gaussian modified with Hermite polynomials (h3, h4, and superior order terms when the signal-to-noise ratio of the data is large enough to allow it), where the latter constrain the deviation of the velocity distributions from a pure Gaussian function.

$$\mathcal{L}(y) = \frac{\exp\left(-y^2/2\right)}{\sigma\sqrt{2\pi}}\left[1 + \sum_{m=3}^{M} h_m H_m(y)\right], \qquad y = (v - V)/\sigma. \tag{4.3}$$

Obviously, if the first two polynomials H_m of the Gauss-Hermite parametrization H_3 and H_4 are close to zero the LOVSD is close to a Gaussian.

$$H_3 = \frac{y\left(2y^2 - 3\right)}{\sqrt{3}}, \qquad H_4 = \frac{4\left(y^2 - 3\right)y^2 + 3}{\sqrt{24}}. \tag{4.4}$$

In particular H_3 describe the skewness: the asymmetric deviations of the line profile from a Gaussian, while H_4 describe the Kurtosis, which is a measure of whether the data are heavy-tailed or light-tailed relative to a normal distribution.

4.1.2 Analysis

For a reliable and unbiased extraction of kinematical information from the spectra, a minimum S/N is required, since the extraction of the LOSVD involves non-linear processes. This makes a spatial re-binning procedure essential to improve

the S/N at the expenses of spatial resolution thus allowing a reliable extraction of the stellar kinematics.

We made use of the adaptive 2D-binning procedure using the "Voronoi Binning" code from Cappellari (Cappellari & Copin 2003). The Voronoi Bins are defined to have a four quadrant symmetry around the photometric center and the quadrants extend along the major and minor axis of the galaxy. For NGC 7619, the signal to noise has been set at $S/N = 70$ and we then extract spectra in 320 bins, while for NGC 1332, we set $S/N = 160$, obtaining 204 bins. In the following figures, the major axis of the galaxies is the horizontal axis and the minor is the vertical one, thus involving a rotation with respect to the original orientation of the datacube on the sky. The bin map obtained from the Voronoi binning code can be seen in Figure 4.1 and in Figure 4.2, for NGC7619 and NGC1332 respectively.

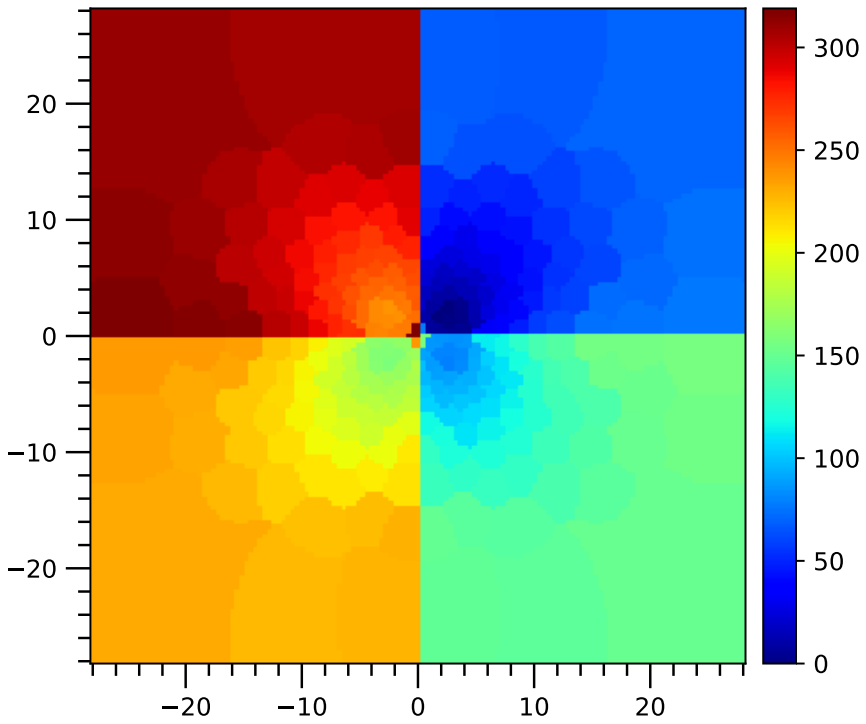

Figure 4.1: Map per bin for NGC 7619 after applying a radially symmetric Voronoi binning scheme with target $S/N = 70$

For the fitting of the kinematical parameters, I have used the Penalized Pixel-

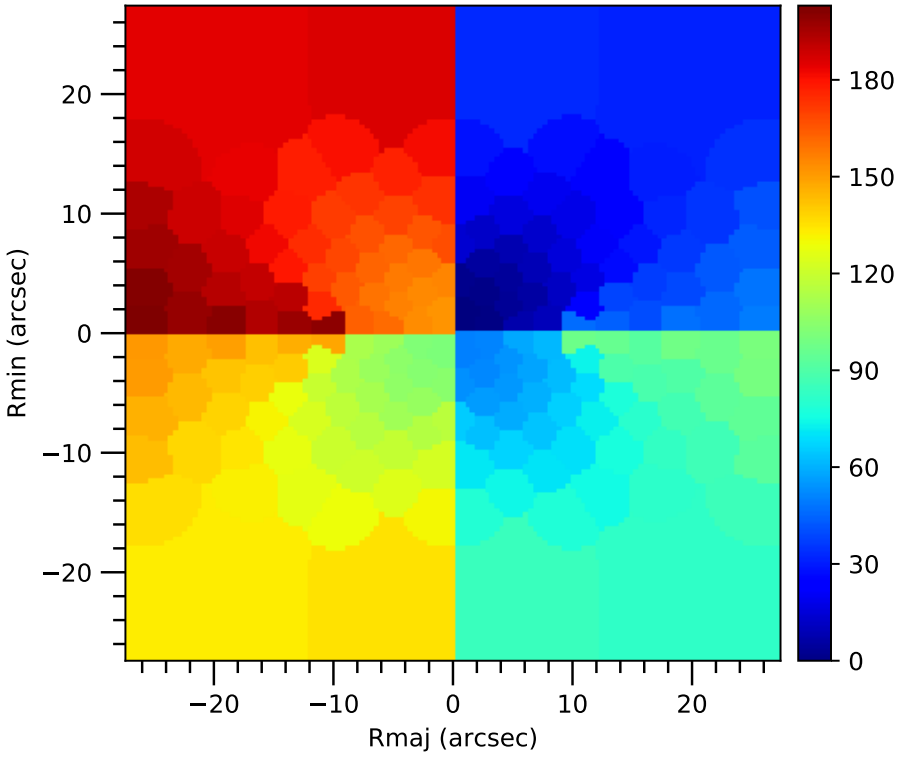

Figure 4.2: NGC 1332 Map per bins after applying a radially symmetric Voronoi binning scheme with target $S/N = 160$

Fitting(pPXF) code presented in Cappellari & Emsellem (2004). This code can be used to extract the stellar kinematics and also the stellar populations by fitting stellar spectra of galaxies (full spectral fitting techinque), using a maximum penalized likelihood approach and it was originally released in 2004 and constantly upgraded through the years (Cappellari 2017). This code approximates the observed galaxy spectrum via the following parametrization:

$$G_{\rm mod}(x) = \sum_{n=1}^{N} w_n \left\{ [T_n(x) * \mathcal{L}_n(cx)] \sum_{k=1}^{K} a_k \mathcal{P}_k(x) \right\} + \sum_{l=0}^{L} b_l \mathcal{P}_l(x) + \sum_{j=1}^{J} c_j S_j(x), \quad (4.5)$$

Where $\mathcal{P}_k$ and $\mathcal{P}_l$ are multiplicative or additive orthogonal polynomials of de-

gree k and l respectively, S_j are the spectra of the sky and T_n are the templates convolved as they had been observed with the same spectral resolution as the galaxy.

A key feature of pPXF, from which the method derives its name, is the fact that it automatically penalizes non-Gaussian solutions to reduce the noise in the recovered kinematics when the data do not contain sufficient information to constrain the full shape of the LOSVD. This is done by minimizing a new objective function

$$\chi^2_{\rm p} = \chi^2 + \alpha\,\mathcal{P}, \tag{4.6}$$

Where $\mathcal{P}$ is a penalty function that describes the deviation of the LOSVD from a Gaussian shape, and α is an adjustable penalty that depends on the data quality.

In Fig.4.3 I show the output of the fitting procedure for the Bin160 of NGC 1332 as an example of he procedure. This is close to the center of the galaxy where the stellar continuum is bright. However, since the S/N in the Voronoi bins is constant, we have results of similar quality for the others spectra. The only exception is represented by the outermost ring of bins. The low flux in these regions implies a low signal to noise per pixel in the original datacube, which in turn makes reaching the target S/N more difficult and possibly less reliable. In the Figure we can see the input spectrum in black and the fit in red, while green points represent the residuals and the green lines the outliers. The degree of the multiplicative polynomials and the order for the moments selected are also displayed. The adopted values have been selected after some tests, on the basis of better fitting quality. I have then derived the maps of the rotational velocity in the bins, which are shown in Figure 4.4 for NGC 7619 and in Figure 4.5 for NGC 1332.

In both maps it is easy to see the galaxy rotation along the major axis, with velocities values consistent with the literature (see Pu et al. 2010 for NGC 7619 and Rusli et al. 2011 for NGC 1332). The velocity map for NGC 1332 (going from -300 to $300 Km/s$), present much higher rotations velocities than NGC 7619, indeed the former is an S0 galaxy and therefore we expect higher rotational velocities compared to the latter which is morphologically classified as Elliptical, although a quite rotating one.

The maps of velocity dispersion obtained with pPXF are shown in Figures 4.6 and 4.7. They present a typical radially decreasing profile in both cases with a maximum value of $320 Km/s$ in the center of NGC 7619 and a maximum value of $300 Km/s$ for NGC 1332. Both these results are also in agreement with previous literature (Pu et al. 2010; Rusli et al. 2011), although we note a small tension with previous observations in the core of NGC 7619, as discussed below.

The maps of the Hermite polynomials H3 are in Fig.4.8 and H4 and in Fig.4.10, for NGC 7619, and in Figure 4.9 and Figure 4.11. In both cases, H3 and H4 start

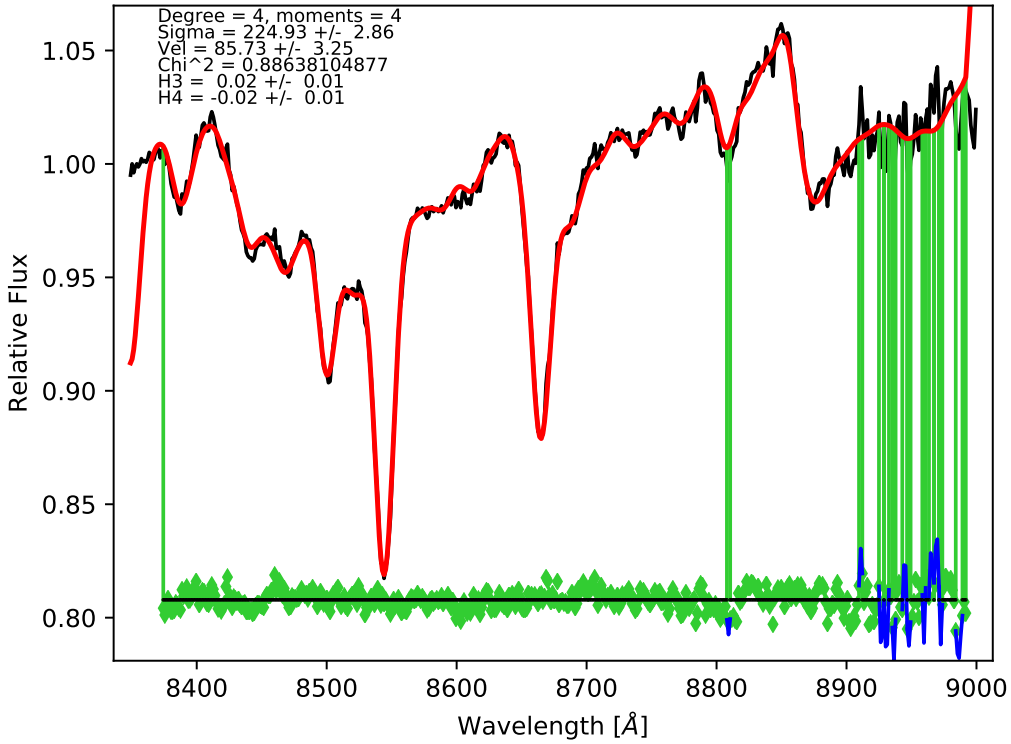

Figure 4.3: PPXF fit for the bin 160 from NGC1332 from MUSE data. The black line is the spectrum of the bins, while the red one is the fitting function. The green points represents the residuals and the blue lines the outliers, connected with the spectra with the green lines. The parameter setting for this fit, as well as the kinematical values obtained, are displayed on the upper left corner of the image.

converging towards zero (i.e. Gaussian LOSVD) when $\sigma_{in} \lesssim \sigma_{inst}$. This displays a small variations of H3 and H4 values: from -0.20 to 0.25 and from -0.25 to 0.20 respectively for NGC 7619, while for NGC1332, from -0.10 to 0.12 and from -0.28 to 0.20. These results provides extra confidence in the correctness of the kinematical analysis.

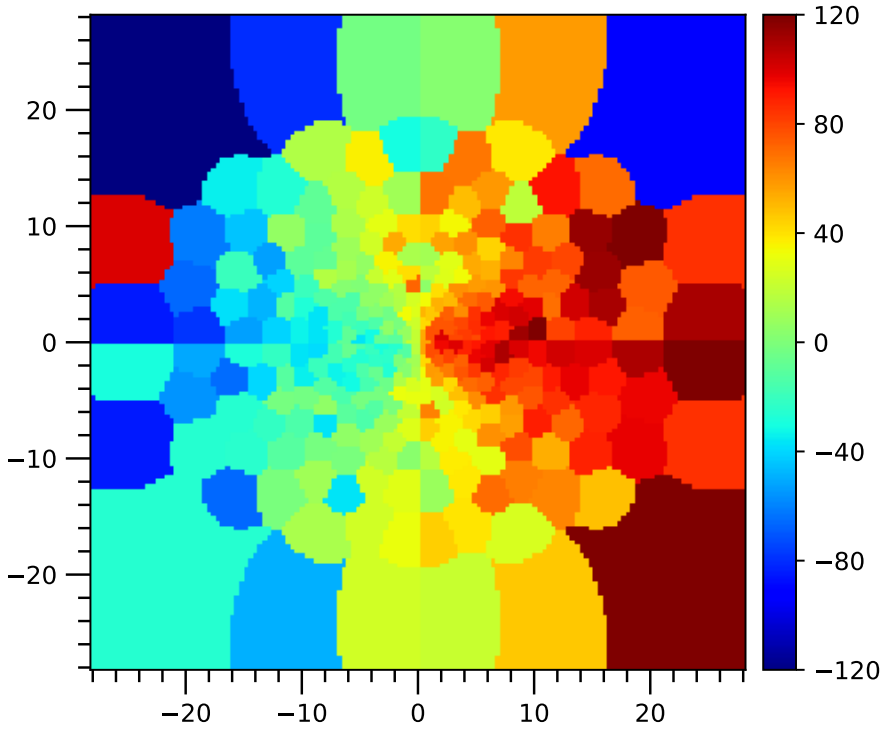

Figure 4.4: Velocity map of NGC 7619 per bins. The galaxy rotates on its major axis with a velocity range of $\pm 120 Km/s$

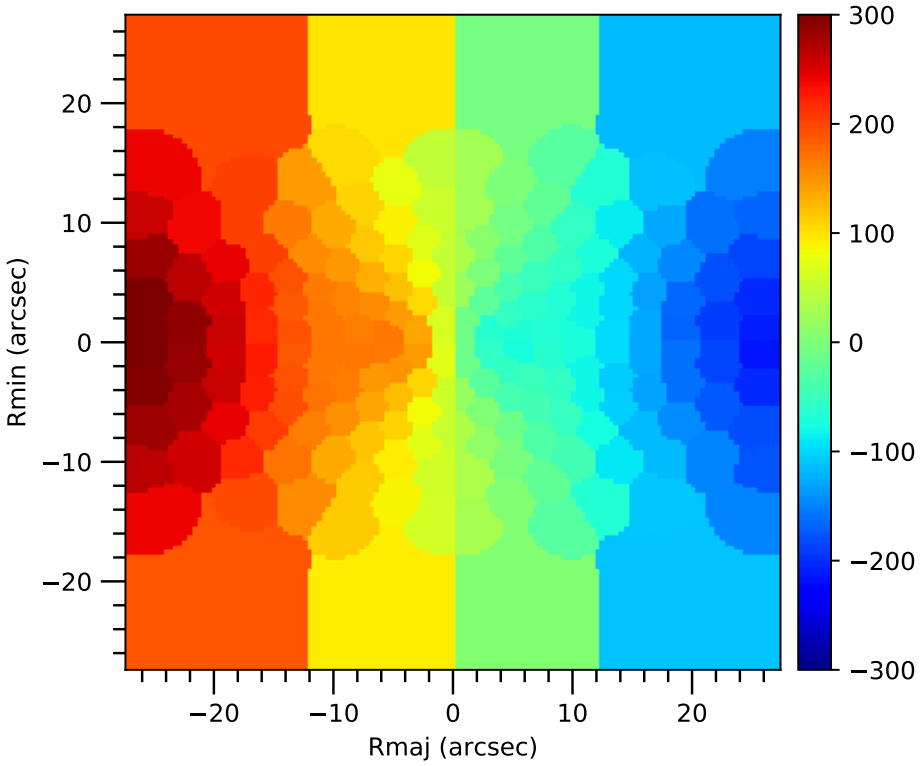

Figure 4.5: Velocity map of NGC 1332 per bins. The galaxy rotates on its major axis with a velocity range of $\pm 300 Km/s$

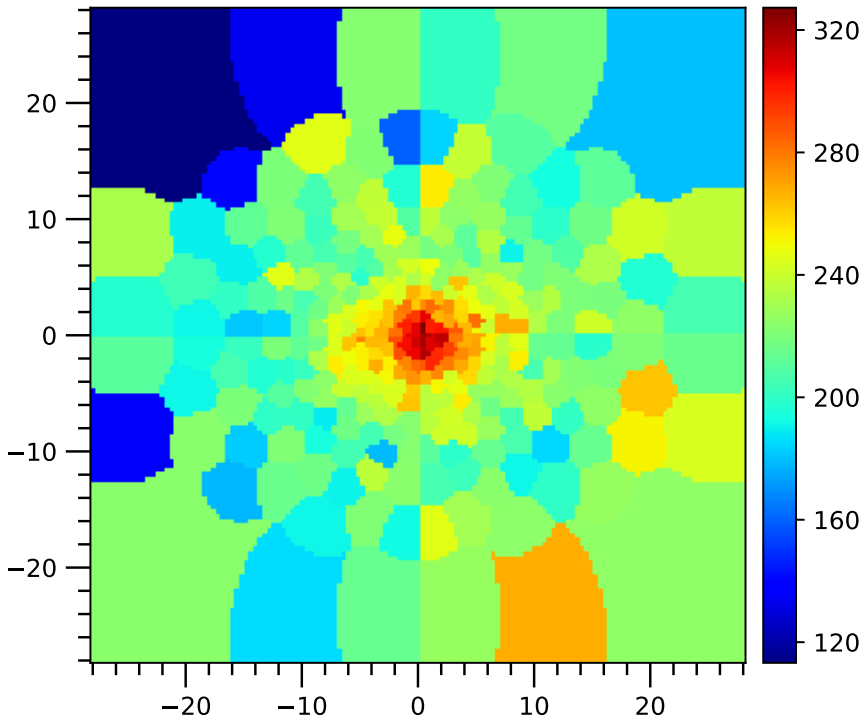

Figure 4.6: NGC 7619 sigma map per bins. The galaxy presents a radial sigma profile with a peak of 300 in the center

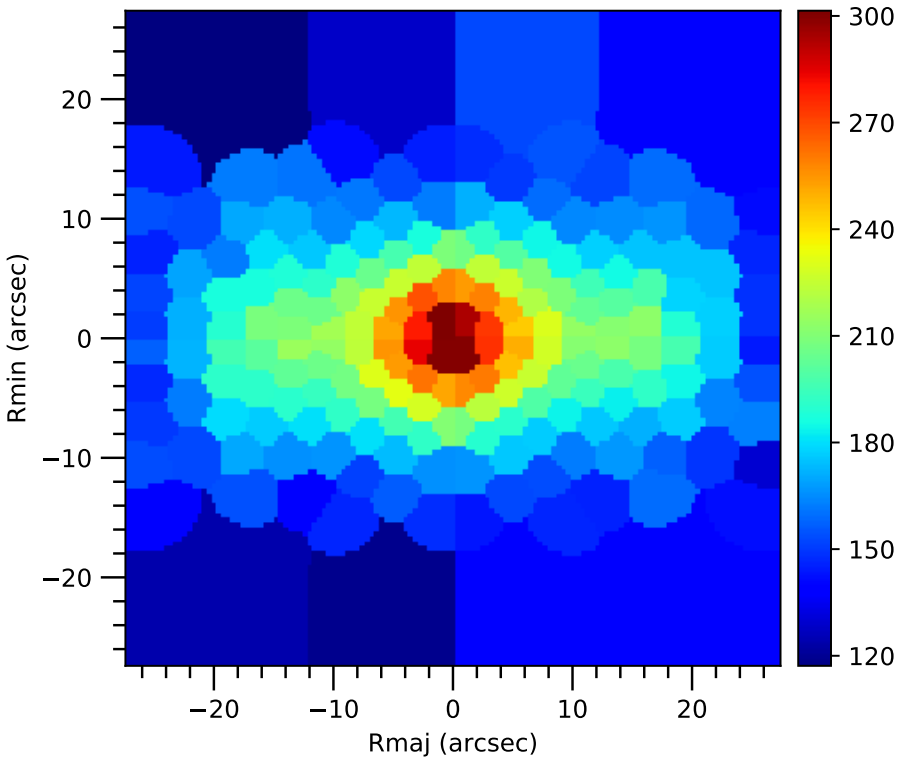

Figure 4.7: NGC 1332 sigma map per bins. The galaxy presents a radial sigma profile with a peak of 320 in the center

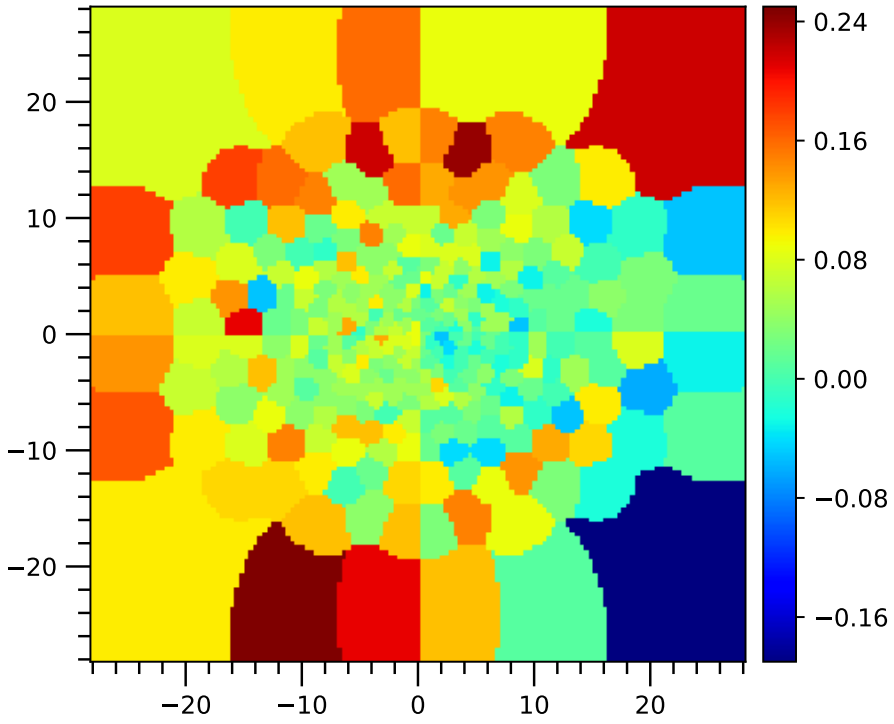

Figure 4.8: Map per bin of the H3 parameter from pPXF of NGC 7619. The value going form -0.2 to 0.24 give us confidence on the reliability of the kinematical results.

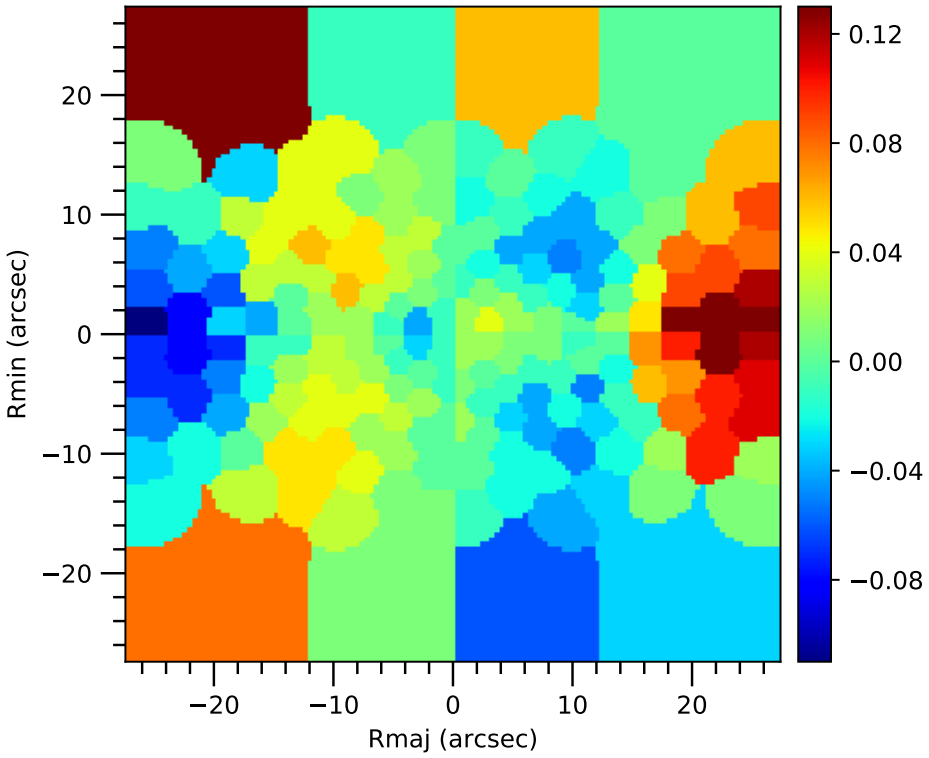

Figure 4.9: Map per bin of the H3 parameter from pPXF of NGC 1332. The value going form -0.1 to 0.12 give us confidence on the reliability of the kinematical results.

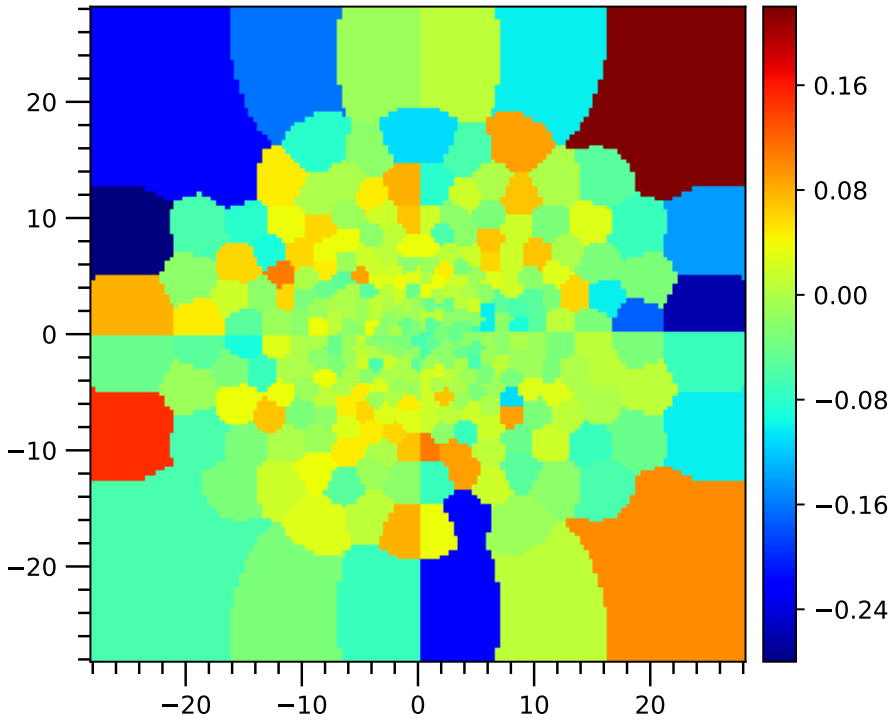

Figure 4.10: Map per bin of the H4 parameter from pPXF of NGC 7619. The value going form -0.26 to 0.2 give us confidence on the reliability of the kinematical results

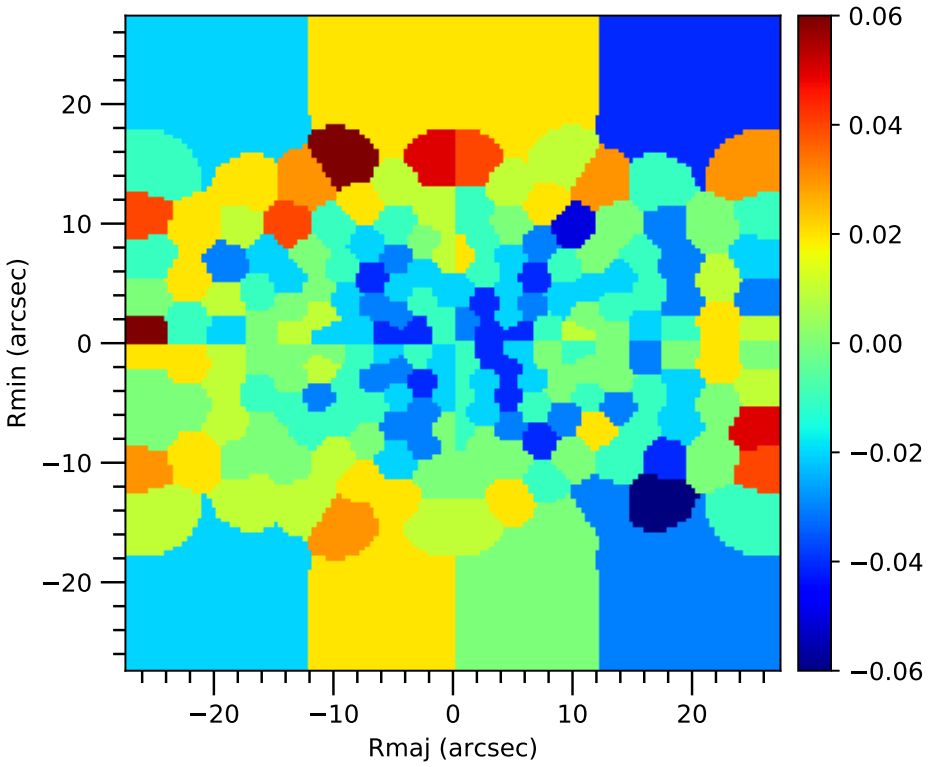

Figure 4.11: Map per bin of the H4 parameter from pPXF of NGC 1332. The value going form -0.06 to 0.06 give us confidence on the reliability of the kinematical results

4.2 Lick indices

4.2.1 Physical Description

A population of young stars with relatively high metallicity has a SED that looks very similar to that of an older population of lower metallicity. This implies that the spectrophotometric properties of an unresolved stellar population are highly similar to those of another population which is for instance three times older and with half the metal content. Using broadband optical colours alone, it is difficult to derive age and metallicities of old stellar populations (Worthey et al. 1994). To overcome this issue, spectral indices have been introduced. From spectral synthesis models it is possible to define several spectral indices, centered on galaxy absorption features, that are sensitive to the age of a certain stellar population and to the abundance of certain elements. Indices of lines from the Balmer series, such as $H\beta$ and $H\delta$ are indeed more sensitive to age, while others from metal lines, like Mgb, $Fe5270$, $Fe5335$, are more indicative of the population's metallicity. Each index is defined by a central band of width $\Delta\lambda_0$ and two sidebands. The central band is used to extract the flux of the absorption feature, while the sidebands are averaged and used to derive the stellar continuum intensity. The index value is an equivalent width measurement. This quantity, of critical importance in spectroscopy, is the width of a rectangle with a height equal to that of continuum emission, such that the area of the rectangle is equal to the area in the central band. Lick indices have been introduced by Faber et al. (1985), and some of their proprieties have been studied by Worthey et al. (1994) and Worthey & Ottaviani (1997), some of them are measured in terms of magnitude while others are measured in terms of equivalent width.

4.2.2 Analysis

The code used to compute lick indices, has been originally developed by Maximilian Fabricius (private comm.). I improved the code with respect to its first version also by adding new features to the index library to cover the extended wavelength range of the MUSE and KMOS data. More notably, the code now correctly works also for spectra with sigma values higher than the Lick system resolution of 220 km s^{-1}. When the resolution is higher than that, the code loads a calibration file from the MILES extended library: the spectrum of a single stellar population with an age of 13.5 Gyr, stellar metallicity and assuming a Salpeter IMF. Tests have shown that the quality of the calibration is not sensitive to the exact choice of this calibration spectrum (Saglia, private comm.). The code uses this additional spectrum to compute the correction needed to bring indices from galaxy spectra with high velocity dispersion to the Lick resolution.

Running this code over the MUSE data we have obtained the measurements shown, for example, for bin 160 of NGC 7619 in Figure 4.12 and for bin 154 of NGC 1332 in Figure 4.13.

In this figure we can see the value measured for every line, while the blue and the red areas represent the continuum part of the spectrum, and the green one the actual line detected. It is possible now to produce a map, for all the indices measured for this study: $Fe5015$, $Hbeta$, $Fe5406$, $Fe5270$, NaI, $Mg1$, MgI, $Mg2$, $CaII1$, $Fe5709$, $Fe5782$, $CaII2$, $CaII3$, $TiO1$, NaD, Mgb, $Fe5335$ and $TiO2$. As an example, in Figure 4.14 and 4.15 are shown the maps obtained for Mgb and $CaII2$ on NGC 7619

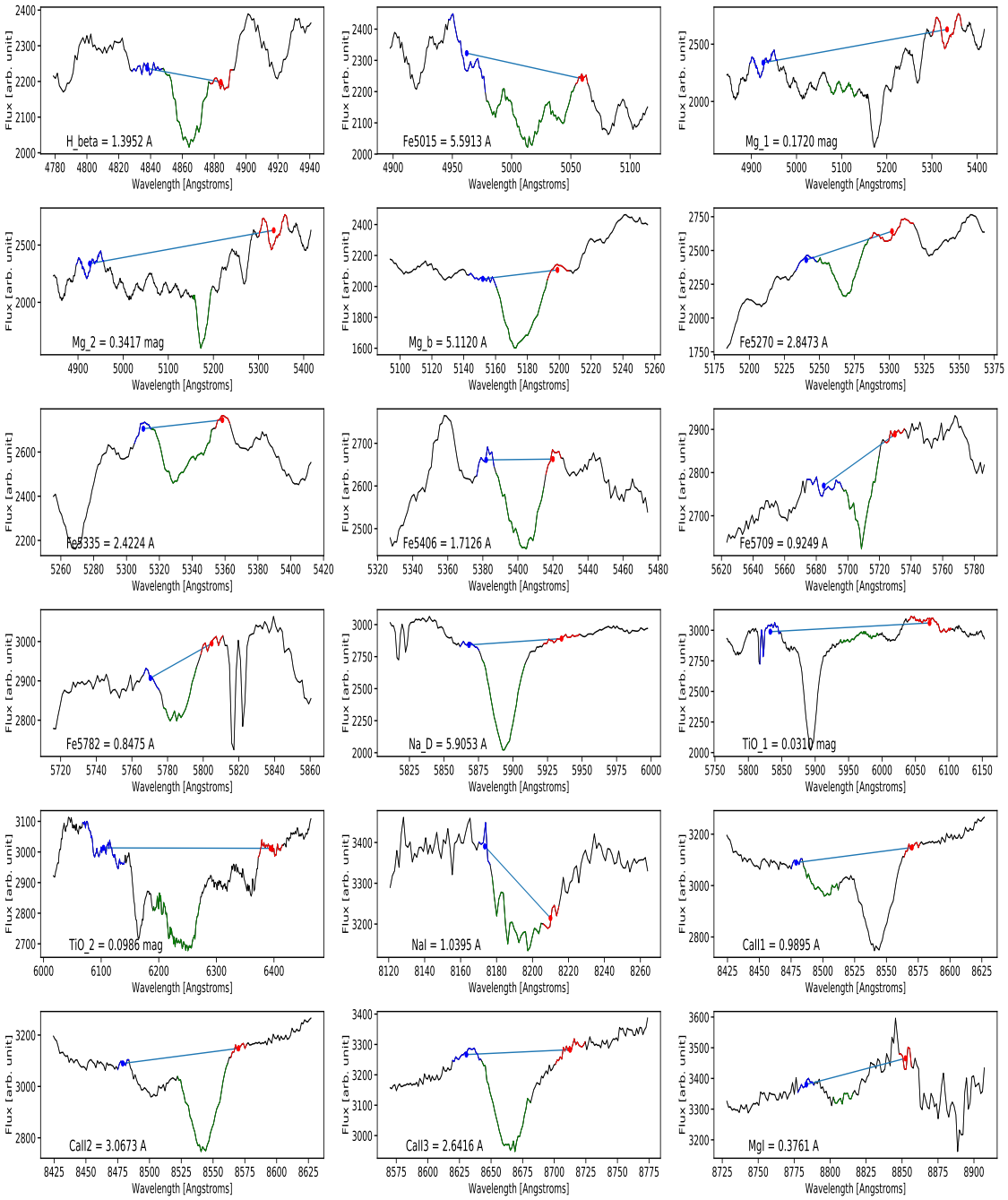

Figure 4.12: NGC7619 indices measurement obtained from bin160. For every panel, the black line is the region of the interest of the spectra, the blue and the red highlighted areas are the detected continuum, and the green one the actual absorption line. The name of the line as well as its measured value is display in the bottom left corner of every panel.

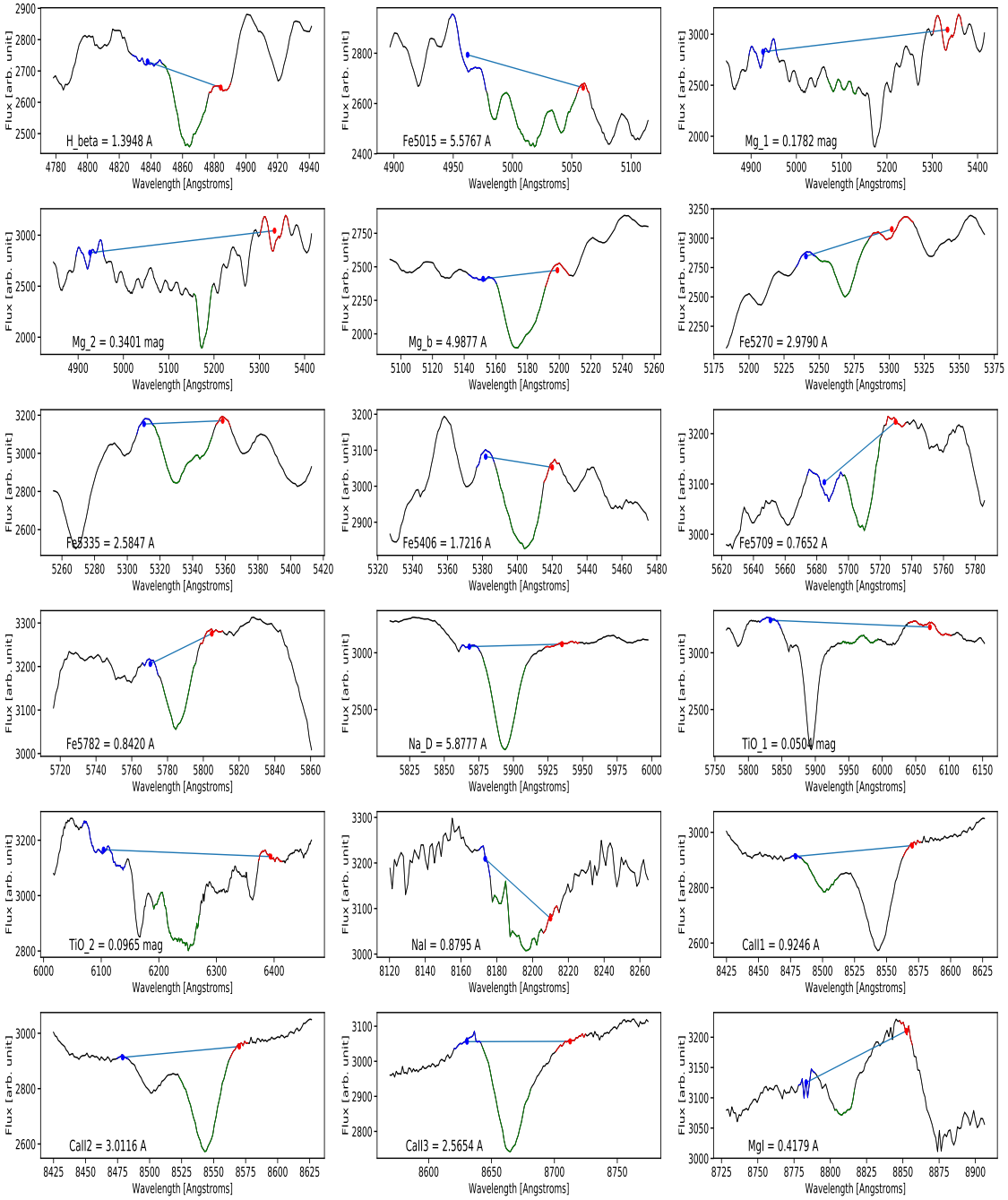

Figure 4.13: NGC1332 indices measurement obtained from bin154. For every panel, the black line is the region of the interest of the spectra, the blue and the red highlighted areas are the detected continuum, and the green one the actual absorption line. The name of the line as well as its measured value is display in the bottom left corner of every panel.

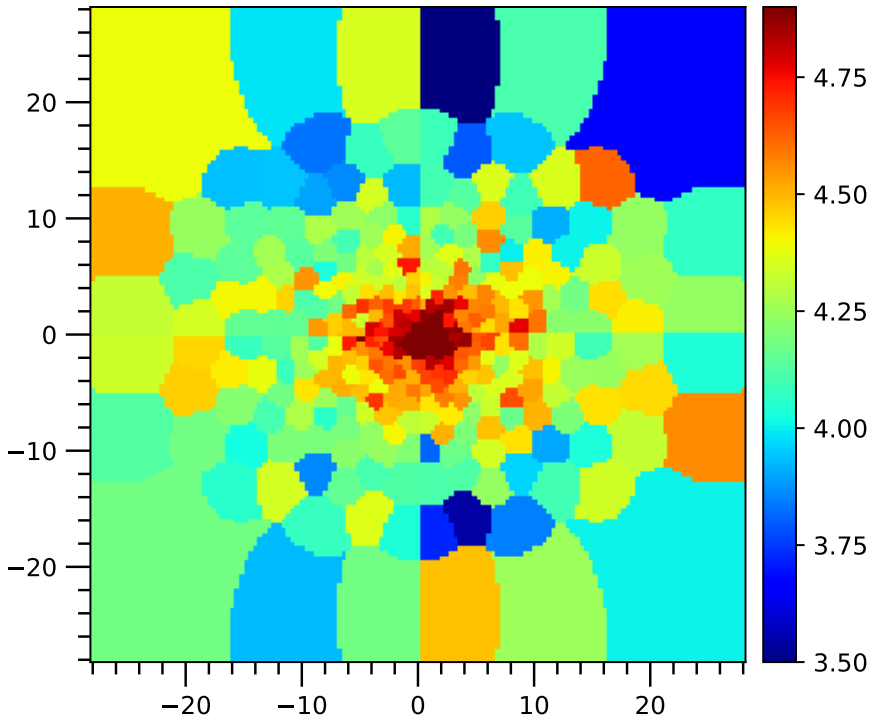

Figure 4.14: bin map of Mgb for NGC 7619 showing a radial profile

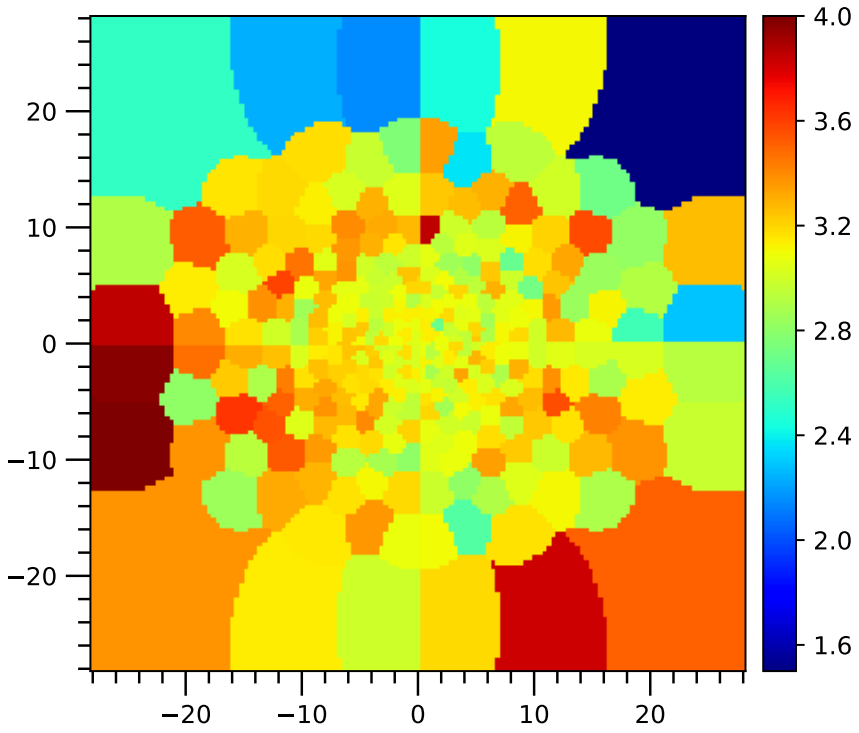

Figure 4.15: bin map of CaII2 for NGC 7619

For the MUSE data of NGC 7619 it also been possible to compare our results for $H\beta$, Mgb, $Fe5015$, $Fe5270$, $Fe5335$ and $Fe5406$ with previous measurements from Pu et al. (2010). The comparisons along the major and minor axis are shown in Figure 4.16 and Figure 4.17. The new data are shown as red dots, while the previous values from Pu et al. (2010) are shown as green dots. There is a general consistency between results, anyhow further tests have shown that the differences in the galaxy nucleus are due to a higher value of sigma presented in Pu et al. (2010). The nature of this difference needs to be investigated on further studies.

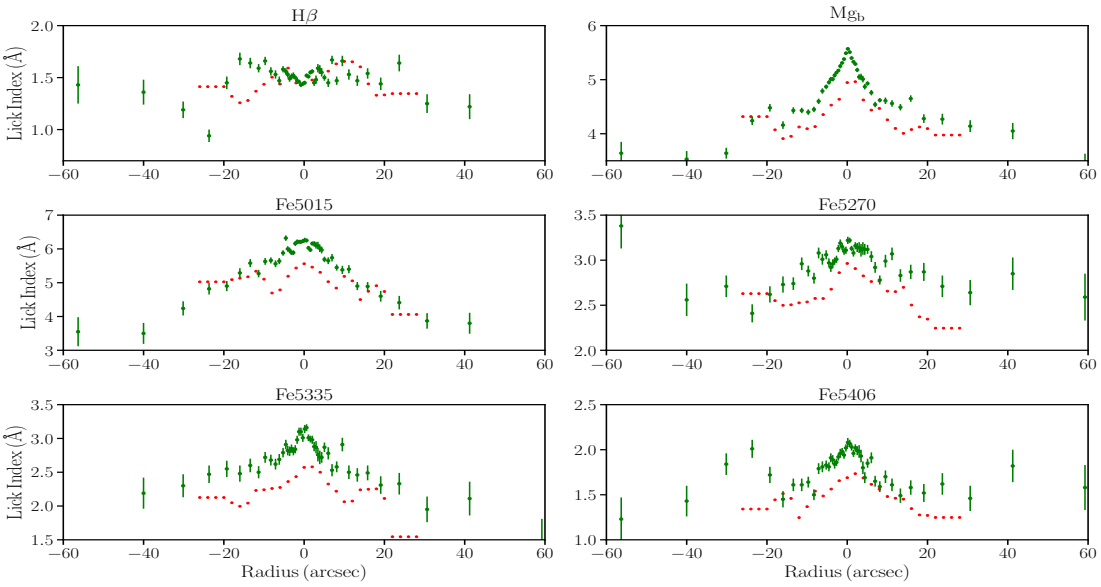

Figure 4.16: Comparison of the indices measured from NGC 7619 with the indices from Pu et al. (2010), on the major axis of the galaxy

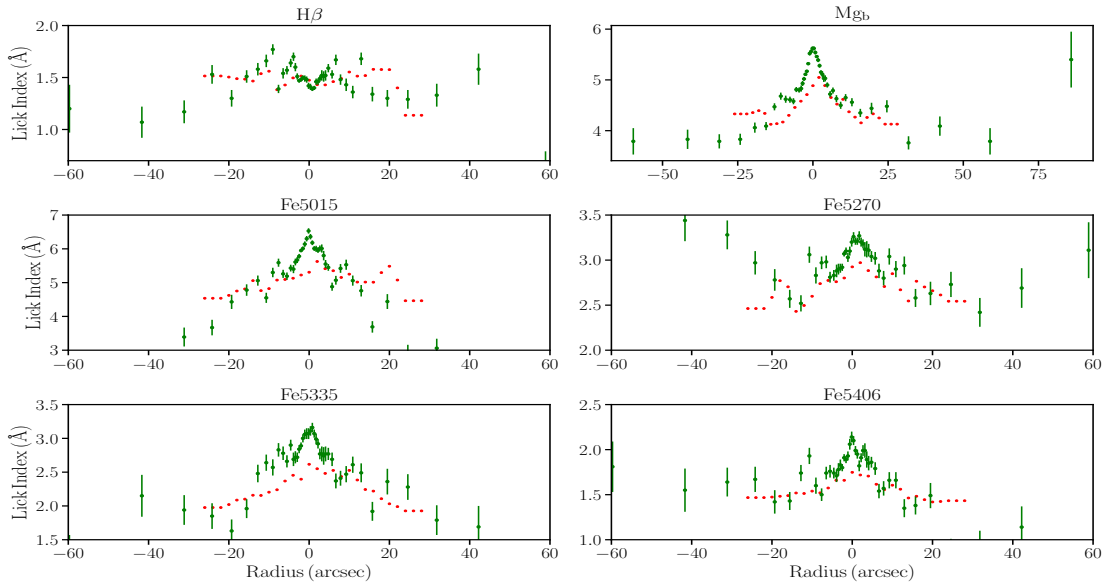

Figure 4.17: Comparison of the indices measured from NGC 7619 with the indices from Pu et al. (2010), on the minor axis of the galaxy

Before measuring the Lick indices for KMOS data, we compared the KMOS spectra with a MUSE spectrum extracted from the inner 2.4 arcsec, equivalent with the area collected from the central IFU in KMOS. For both spectra, this comparison presents different shapes of the continuum of the spectra. Since MUSE has a much higher throughput in this band, and it is less affected by inaccuracies in the sky subtraction, we correct KMOS fluxes with a polynomial multiplicative function using the MUSE data as a reference.The corrections are shown in Figure 4.18 and in Figure 4.19. Even thought this correction improves the Lick's measurements for KMOS data which, as can be seen are in Table 4.1 are in some agreement with the MUSE values, the correction is simply too uncertain outside the overlap area of the two instruments. Moreover the KMOS spectra are affected by significant OH skyline residuals making the determination of the continuum or the band flux less reliable, which in turn is reflected in the quality of the Lick indices measurements, as can be seen in Figure 4.20 for NGC 7619 and in Figure 4.21 for NGC 1332. Hereafter we will focus on the analysis of the MUSE data for the two galaxies in the sample.

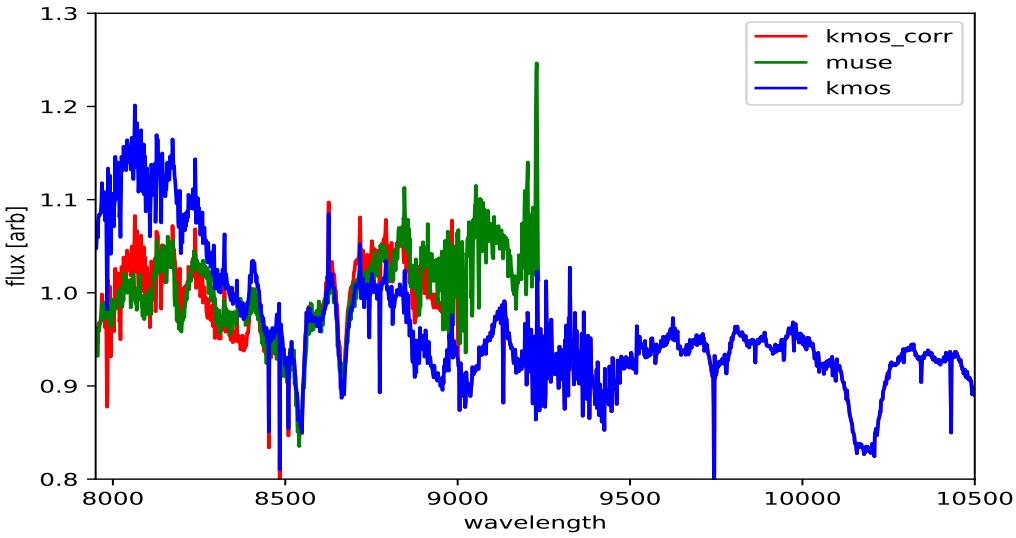

Figure 4.18: Flux of NGC 7619 obtained from MUSE (green), from KMOS (blue) and for the KMOS after the flux correction (red)

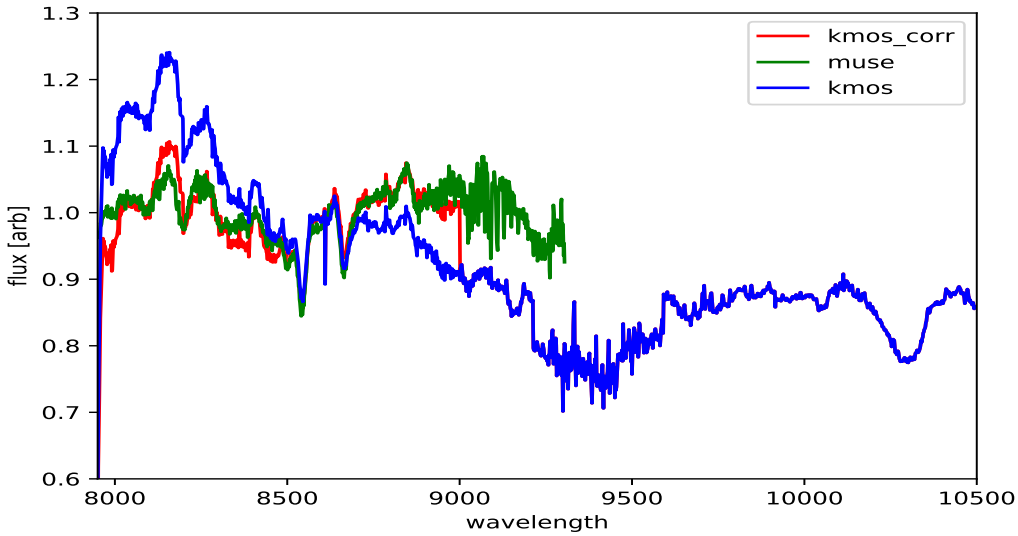

Figure 4.19: Flux of NGC 1332 obtained from MUSE (green), from KMOS (blue) and for the KMOS after the flux correction (red)

Instrument	Object	MgI	NaI	CaII1	CaII2	CaII3	Fe/H
KMOS	1332	0.34	0.35	0.56	2.96	1.95	0.01
MUSE	1332	0.51	0.66	1.00	3.18	2.54	-
KMOS	7619	0.29	0.61	1.01	3.07	3.22	0.34
MUSE	7619	0.39	1.10	1.06	3.03	2.60	-

Table 4.1: Table of the values of the Lick indices (MgI, NaI, $CaII1$, $CaII2$, $CaII3$, Fe/H) for NGC 7619 and NGC 1332 from the overlapping wavelength region between the KMOS IZ and MUSE spectra. The values of the indices are in Å.

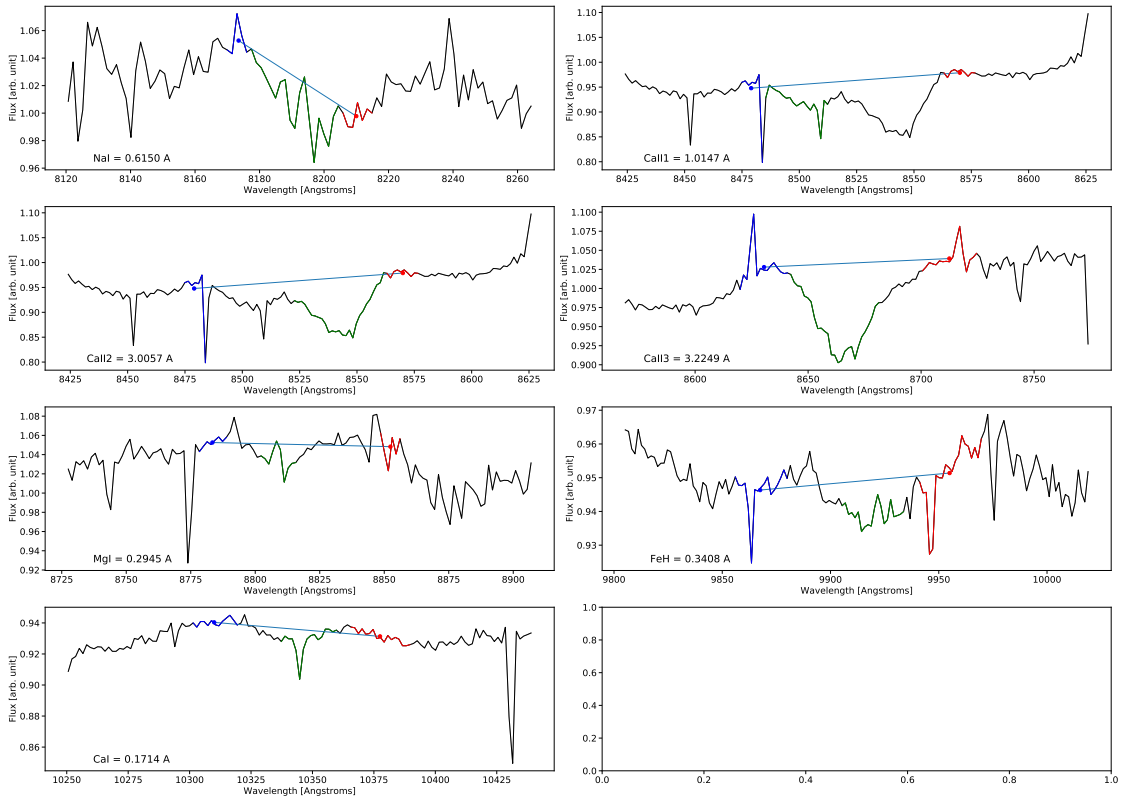

Figure 4.20: NGC 7619 indices measurement obtained from KMOS. For every panel, the black line is the region of the interest of the spectra, the blue and the red highlighted areas are the detected continuum, and the green one the actual absorption line. The name of the line as well as its measured value is display in the bottom left corner of every panel.

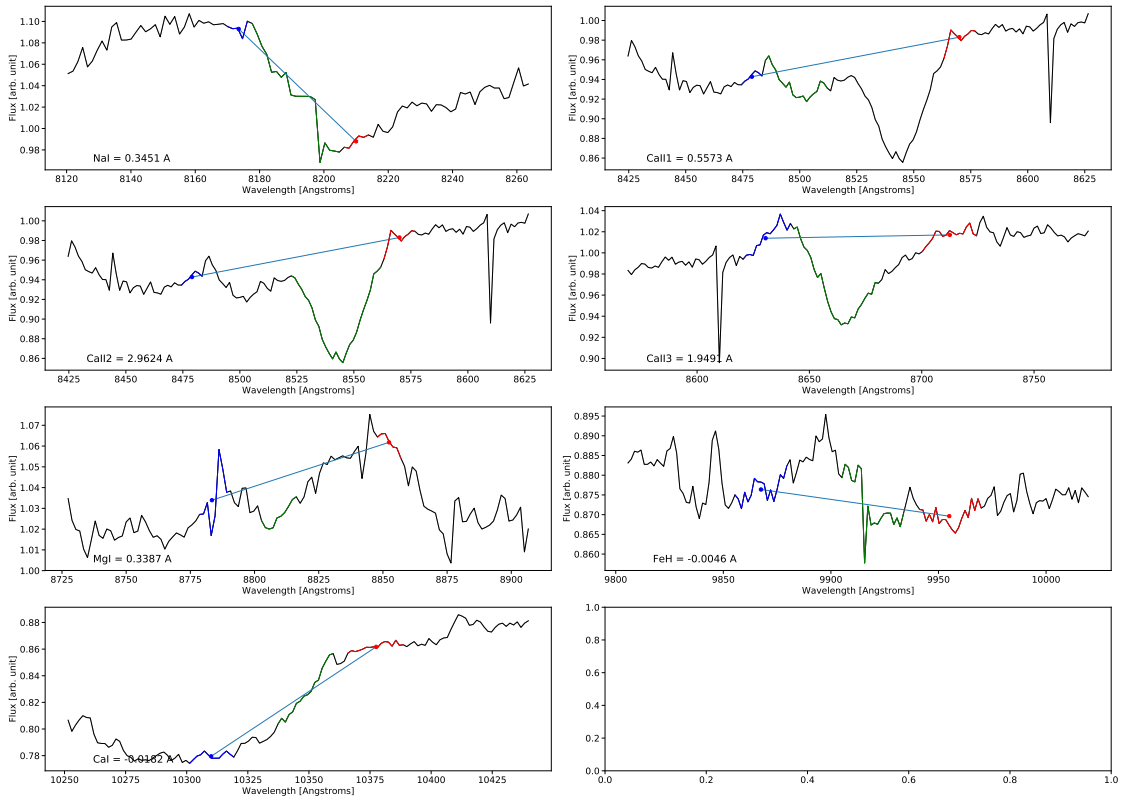

Figure 4.21: NGC 1332 indices measurement obtained from KMOS. For every panel, the black line is the region of the interest of the spectra, the blue and the red highlighted areas are the detected continuum, and the green one the actual absorption line. The name of the line as well as its measured value is display in the bottom left corner of every panel.

4.3 Fitting of the physical parameters

To reconstruct the stellar IMF (see Section 1.4) from our measured line indices, it is necessary to make use of stellar populations models.

A single stellar population (SSP) is a single and coeval star formation event, where the number ratio of stars of different masses follows the adopted IMF. The synthetic stellar population models make use of our knowledge of the stellar evolution via isochrone tables. These describe the evolution of stars on the Hertzsprung-Russel (HR) diagram, and they are composed of evolutionary tracks as a function of mass (M), metallicity (Z), and time (t). From these tables we obtain the spectrum of a star given M, L and t. Then, by summing the spectra for all the stars (weighted by the IMF) is possible to obtain the luminosity spectrum of the stellar population as a function of time. For the purpose of this work, we test three different, publicly available, populations models. The first model we use is from Thomas et al. (2005), it spans a range of α/Fe, Age, and metallicity, with an assumed Kroupa IMF.

Then we make use of the Flexible Stellar Populations Synthesis (FSPS) model (v3.0) from Conroy et al. (2009). The FSPS model synthetically generates a set of stellar populations making use of Padova tracks (Girardi et al. 2000), and a custom model grid has been generated using pyFSPS, a python wrapper of the FSPS code. Our grid has three free parameters. First, we vary the stellar metallicity using the parameter *logzsol* to span a range that goes from sub- to super-solar metallicity: $-0.4 < \log Z/Z_{\odot} < 0.3$ in steps of 0.1.

Second, we set *imftype=2* in the code, that correspond to a Kroupa-like IMF, with this choice we are able to freely vary the slope of the initial mass function in three mass ranges $0.08 < M < 0.5M_{\odot}$, $0.5 < M < 1.0M_{\odot}$, and $1.0 < M < 100M_{\odot}$. The default values for this IMF parametrization are 1.3, 2.3, and 2.3 in the three mass ranges respectively. In order to study the ratio of massive to dwarf stars, we let the slope of the first mass range (*imf1*, $0.08 < M < 0.5M_{\odot}$) to vary from 1.1 to 3.5 in steps of 0.2.

Third, we run models with different SSP ages which go from 4 to 15 Gyr in steps of 0.25 Gyr. With these choices we obtained a library of 5042 model spectra all with fixed $\alpha/Fe = 0$, as it is not possible to change this parameter in the current public version of FSPS.

The third model we use is presented in Conroy & van Dokkum (2012), this model has SSP spectra for a fixed solar metallicity and a fixed age of 13.5 Gyr, while it has the advantage that the $\log \alpha/Fe$ is variable and it can assume the following values: 0 (solar), 0.2, 0.3 and 0.4. At the same time the IMF shape can be varied with the following five choices: $x = 3.5$, $x = 3$, $x = 2.3$, Chabrier IMF and bottom-light IMF (a Salpeter IMF with a flat steepness for low masses),

where x is the slope of the IMF.

From the Conroy et al. (2009) models, it is possible to see the behavior of $Hbeta$, Mgb, $Fe5270$ and NaI as function of the IMF slope for varying ages and metallicity (from 0 to 0.3), at solar α/Fe, as shown in Figure 4.22. Here, the optical indices ($Hbeta$, Mg, Fe) do not strongly depend much on the IMF, but vary as a function of age and metallicity. In contrast, NaI is a strong function of the IMF slope and age, but not so much of metallicity.

We then proceed to explore the dependence of the strengths of the same indices with the IMF slope, at fixed age (13.5 Gyr) and solar metallicity, but this time with variable α/Fe from the Conroy & van Dokkum (2012) models. This dependencies are shown in Figure 4.23. Lines of different colors correspond to different values of α/Fe as labeled in the panels. It is immediately obvious that the strength of Mgb and $Hbeta$ does depend on the α overabundance but not on the IMF slope. The NaI index does depend on the element overabundance but also shows the strongest dependence on the IMF slope, while the Fe index is relatively independent from these quantities. Therefore, the NaI index is a good indicator for studies of the IMF slope. However, an accurate characterization of it requires good estimates of the α overabundance and the metallicity (Fe/H), although we cannot explore the dependence on this latter parameter here because the Conroy & van Dokkum (2012) models do not allow us to vary the metallicity above the solar value.

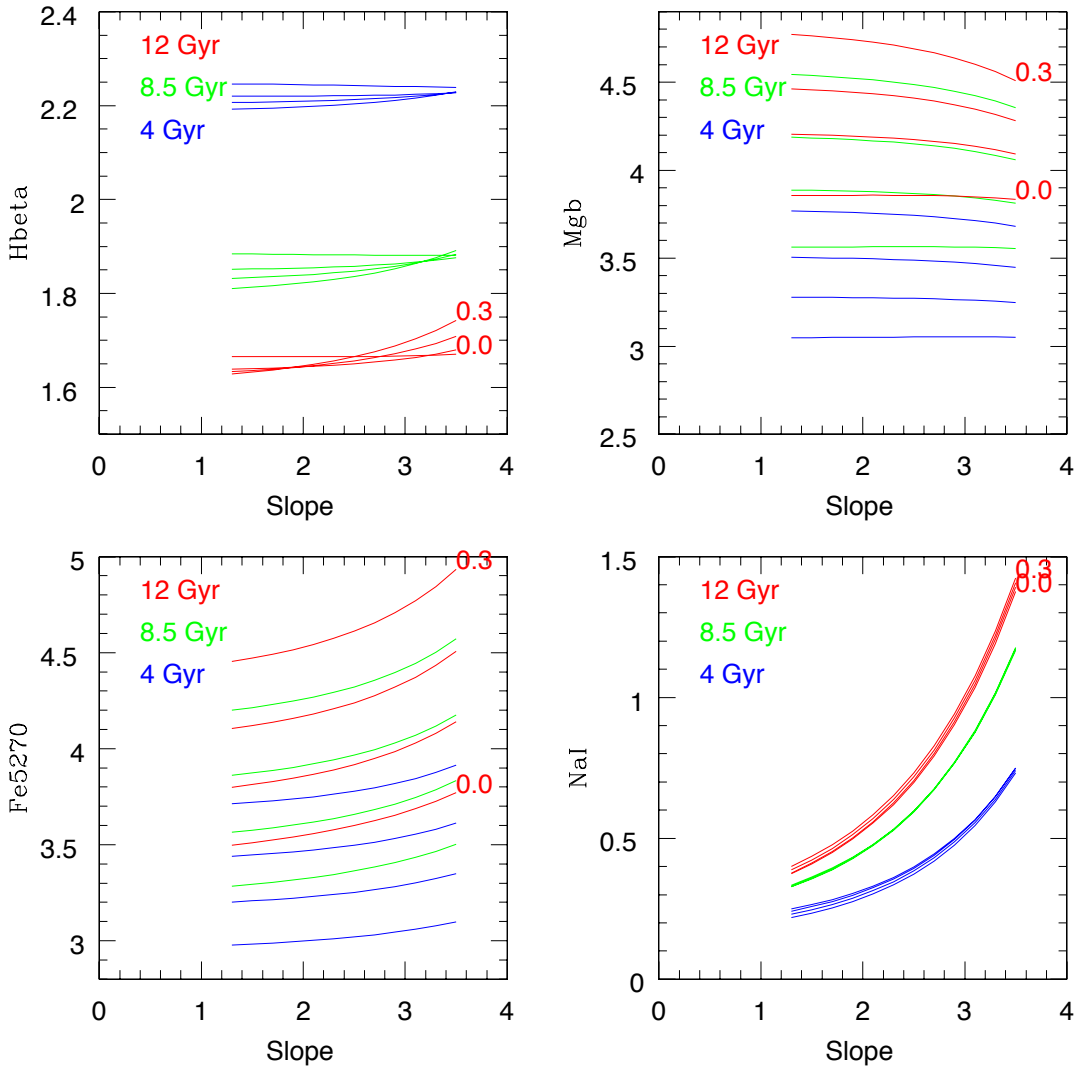

Figure 4.22: $H\beta$, Mgb, $Fe5270$ and NaI as function of the IMF slope, for varying ages, (displayed in different colors for different values of α/Fe) and metallicities. Obtained from Conroy et al. (2009) models, with a fixed solar α/Fe.

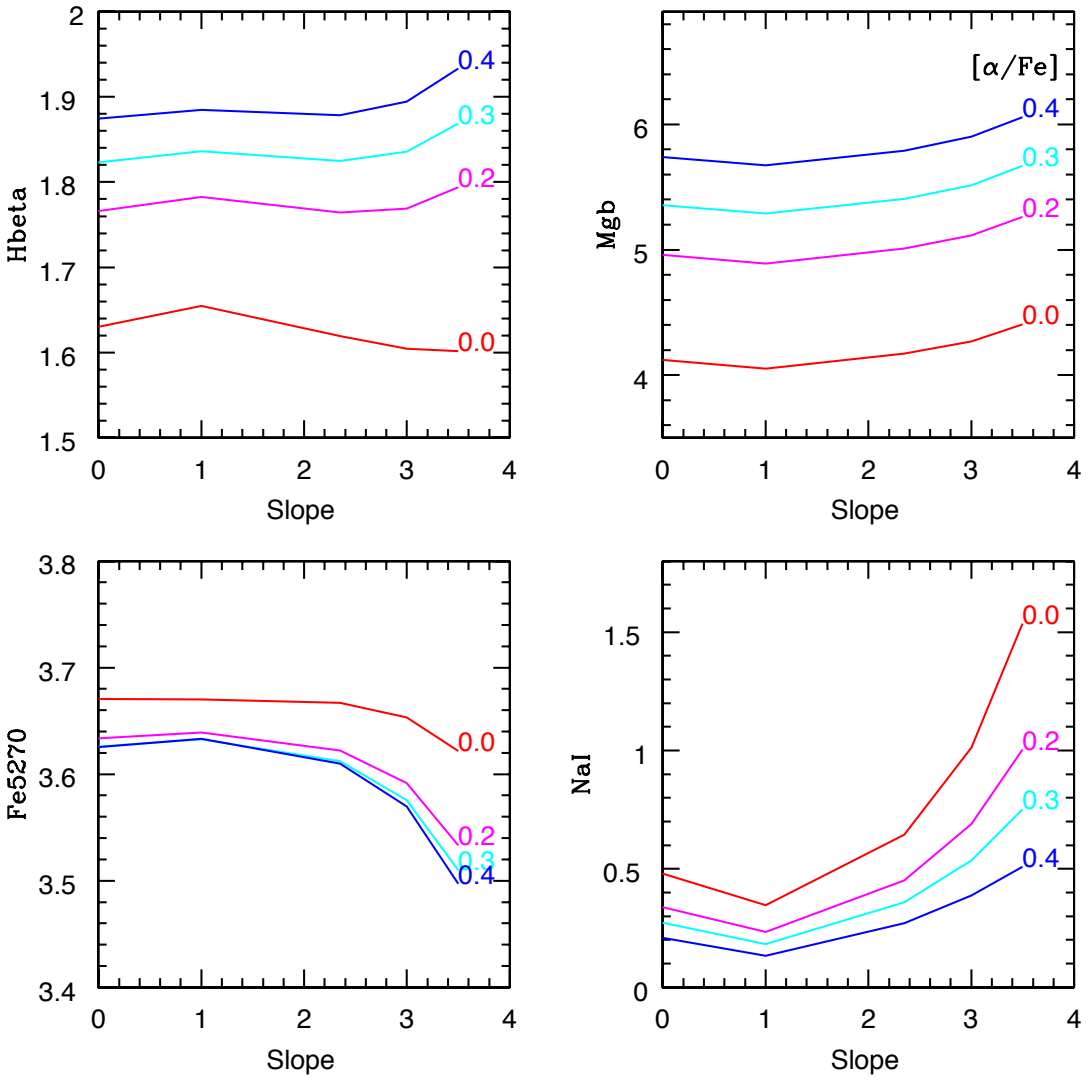

Figure 4.23: *Hβ*, *Mgb*, *Fe*5270 and *NaI* as function of the IMF slope, for varying solar abundances, displayed in different colors. Obtained from Conroy & van Dokkum (2012) models, with a fixed age of 13.5*Gyr* and solar metallicity.

Focusing on NGC 1332, we fit our measurements of the Lick indices (as a function of galaxy radius) with the models from Thomas et al. (2005). As can be seen in Figure 4.24, we have obtained a high SSP age (> 13 Gyr), indicative of an old galaxy which is metallicity enriched in the center (where the bulge dominates) and less in the outer parts (where the disk dominates). It is also overabundant in α elements and presents a $M/L \simeq 5$ slightly higher than the value previously measured dynamically by Rusli et al. (2011), but still in good agreement with the Kroupa IMF parametrization. We then proceed fitting the NaI index with the models with the free IMF parametrization, free metallicity, but fixed solar α abundance from Conroy et al. (2009), obtaining a Kroupa like IMF even in this case of direct fitting of the IMF slope, as can be seen in the bottom panel of Figure 4.25. However, the value of NaI shown in the top panel of the same Figure, is too high for the models with α overabundance, from Conroy & van Dokkum (2012).

Going through the same fitting for NGC 7619 from Thomas et al. (2005) models,as can be seen in Figure 4.26, we have obtained even for this galaxy an old stellar population, mainly driven by the $Hbeta$ strength. From the values of the Fe and Mgb indices we find that also this object is metal rich (reaching 2 times the solar metallicity in the inner bulge) and α overabundant. The M/L ratio of $\simeq 3.5$ in the I band with a Kroupa IMF matches the dynamical value determined by Rusli et al. (2013) for this galaxy. Even here, NaI index can only be fitted with a Conroy model with solar alpha abundance from Conroy et al. (2009), shown in 4.27, presenting an IMF slightly steeper than Kroupa. However, the NaI is still too high for the Conroy & van Dokkum (2012) models with α overabundance.

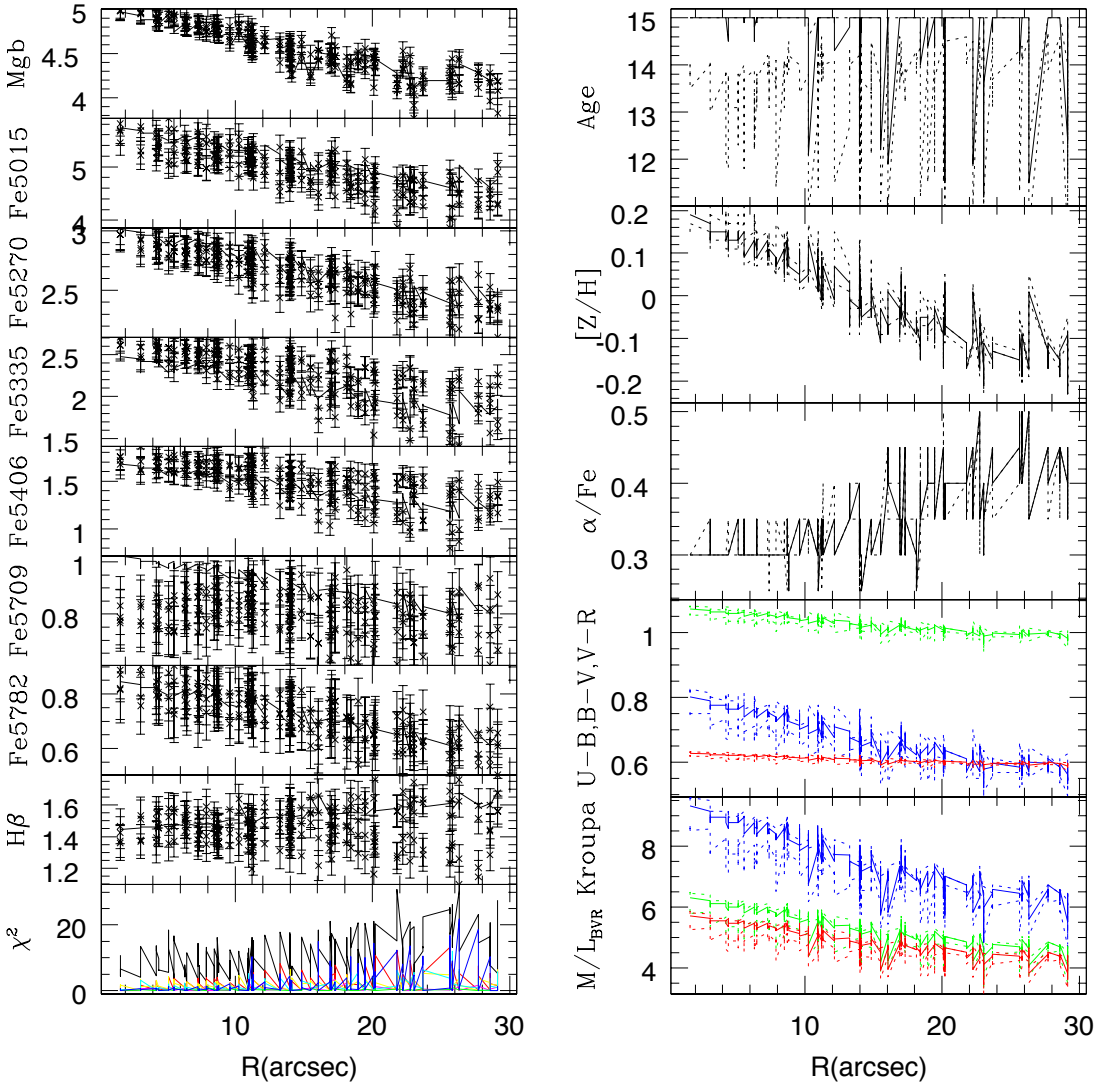

Figure 4.24: On the left panel, the main absorption line measurements for NGC 1332, as function of the radius. On the right panel, the corresponding physical proprieties obtained from Thomas et al. (2005) models as a function of the radius. The $H\beta$ on the left panel is a direct indicator of the age displayed on the top right panel as well as the ratio between the strength of the Fe indices and $H\beta$ define the Z/H behavior. The ratio between Fe indices and Mgb define the α/Fe trend. The bottom left panel represent the χ^2 and the last two panels on the right side represent respectively the color indices and M/L ratio for a Kroupa IMF.

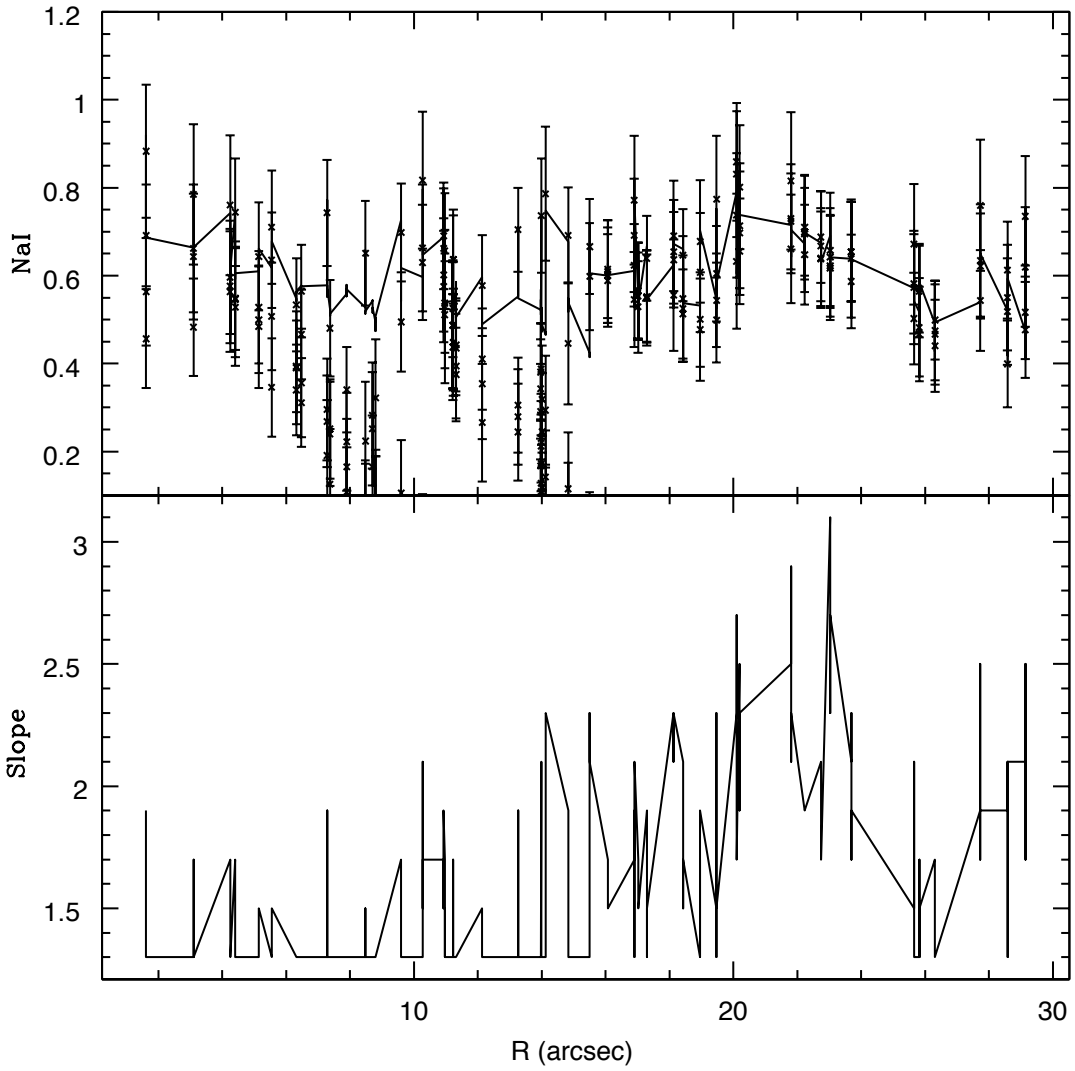

Figure 4.25: *NaI* mesaurement on the top panel and slope of the IMF on the bottom, both as a function of the radius for NGC 1332, obtained from Conroy et al. (2009) models. The corresponding IMF slope with the value of *NaI* detected, correlate with a Kroupa IMF.

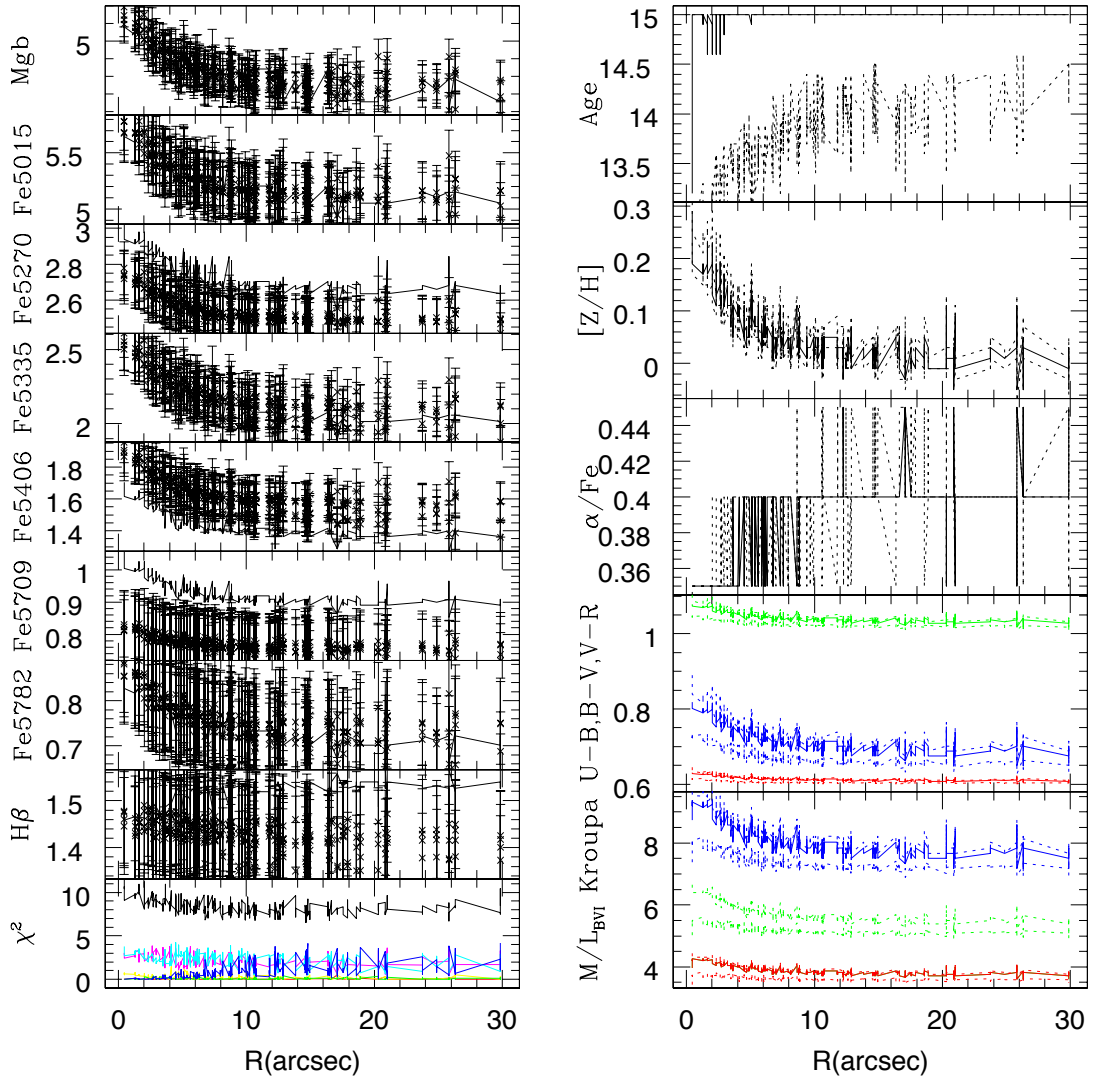

Figure 4.26: On the left panel, the main absorption line measurements for NGC 7619, as function of the radius. On the right panel, the corresponding physical proprieties obtained from Conroy et al. (2009) models as a function of the radius. The $H\beta$ on the left panel is a direct indicator of the age displayed on the top right panel as well as the ratio between the strength of the Fe indices and $H\beta$ define the Z/H behavior. The ratio between Fe indices and Mgb define the α/Fe trend.The bottom left panel represent the χ^2 and the last two panels on the right side represent respectively the color indices and M/L ratio for a Kroupa IMF.

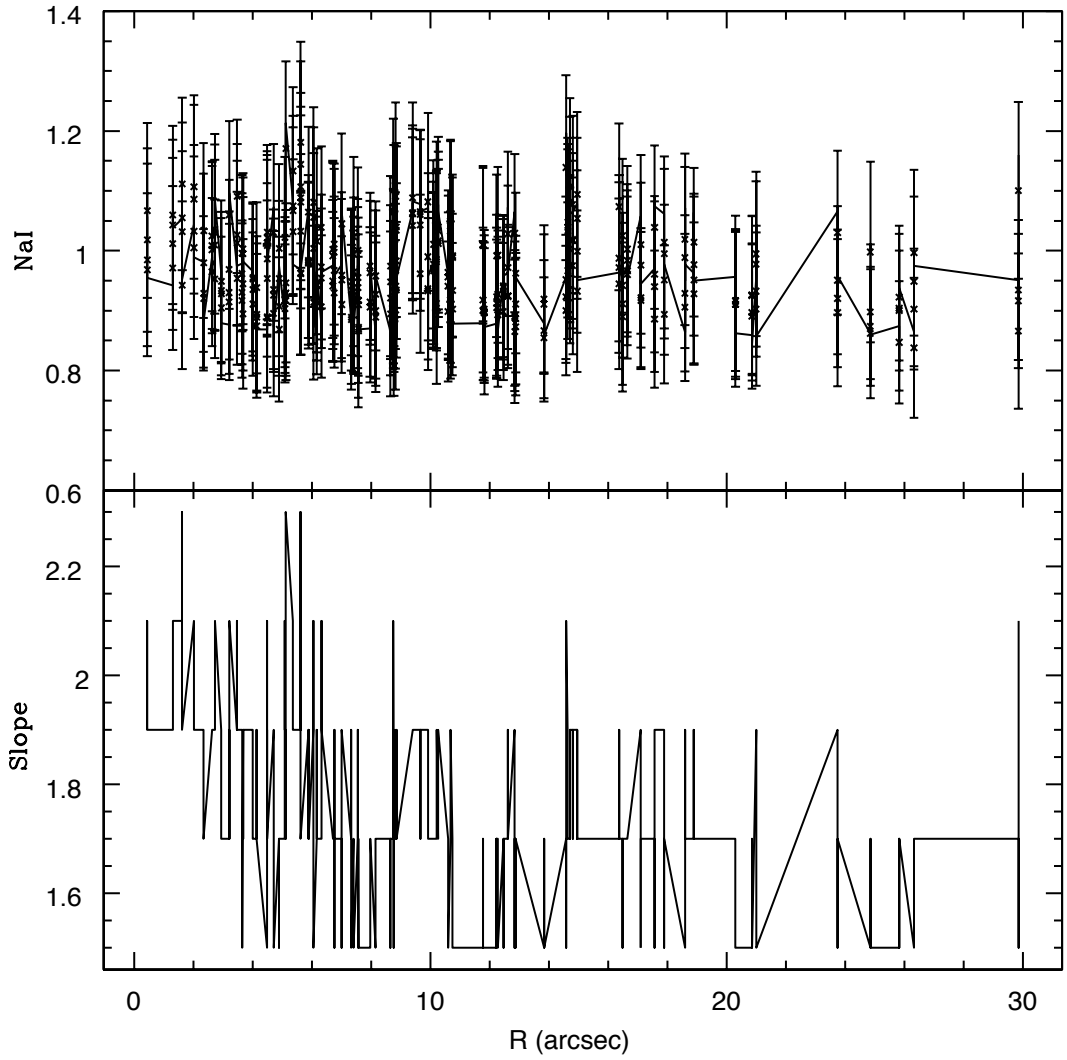

Figure 4.27: *NaI* measurement on the top panel and slope of the IMF on the bottom, both as a function of the radius for NGC 7619, obtained from Conroy et al. (2009) models. The corresponding IMF slope with the value of *NaI* detected, correlate with a Kroupa IMF.

In summary, both galaxies could be compatible with a Kroupa-like IMF, both from the dynamical and the indices analysis. However, one needs to assume that the Na abundance does not decrease when the abundance of α elements increases, contrary to what Conroy's models predict. Indeed, Conroy's models match with the simple expectation that the Na abundance should decrease with increasing α/Fe because Na is not an α element. Therefore at fixed metallicity, an increased fraction of α elements turns into a lower fraction of non-α elements.

To further investigate this behaviors in different models, we produce in Figure 4.3 the NaD index as predicted by the models of Thomas et al. (2005) and the ones of Conroy et al. (2009). Here is easy to see that the first do not vary as a function of alpha overabundances, while the second do. To allow a definitive study of the IMF slope, in further studies, we need new and more complete models that allow a self-consistent treatment of variable metallicities, α overabundances, IMF shape and SSP age; a task not possible with current publicly available stellar population models.

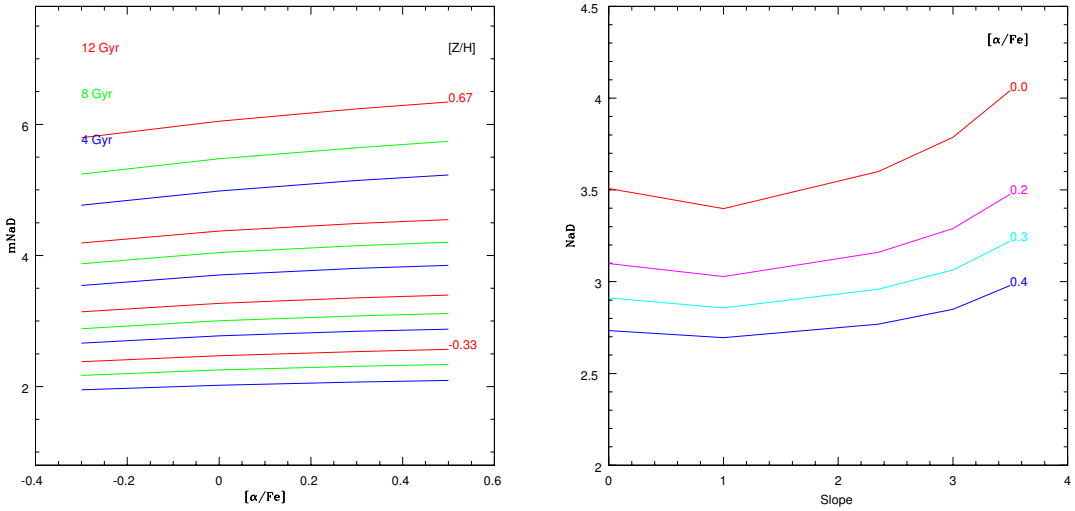

Figure 4.28: On the left panel is displayed the NaD strength as a function of α/Fe for different ages shown in different colors, obtained from, Thomas et al. (2005) models. On the right panel, NaD as function of the IMF slope for varying abundances displayed in different colors, obtained from Conroy et al. (2009) models with fixed age and metallicity. In this figure we note the strong dependence of the NaD absorption line with α/Fe in the Conroy et al. (2009) models, while in the Thomas et al. (2005) models this index is insensitive to the α/Fe parameter.

Chapter 5

Summary and Conclusions

In this work, we have studied two giant Early-Type galaxies, NGC 1332 and NGC 7619, in order to investigate the radial variations, if any, of the initial mass function. The sample is made of NGC 7619, an elliptical galaxy with a central photometric core, and NGC 1332 which is an S0 galaxy with a massive central bulge.

We performed this study using two integral field spectroscopy instruments, KMOS and MUSE, both mounted on the 8.2m ESO Very Large Telescope. From these observations, we have been able to perform a detailed kinematic study of NGC 7619 and NGC 1332 making use of the pPXF code from Cappellari & Emsellem (2004). With this code, we have derived the line of sight velocity distributions in two dimensional Voronoi bins covering the inner square arcminute around the galaxy center from the MUSE data; as well as in the inner 9 square arcseconds from the KMOS data. Unfortunately, due to the low throughput of KMOS in the IZ band, where we have collected the data, the spectra obtained from KMOS data did not present enough reliability to perform a measurement of the absorption lines, even after a flux correction based on the MUSE spectra as reference. The maps of the rotational velocities show that both galaxies rotate along their major axis, and their velocity dispersions show a clear gradient towards higher values in the center, with value consistent with previous kinematic studies (Pu et al. 2010; Rusli et al. 2011).

With the kinematical parameters in hand, we computed the Lick indices on a series of absorption lines of interest (*Hbeta*, *Mg*, *CaII*1, *CaII*2, *CaII*3, *Hbeta*, *Mgb*, *Fe*5015, *Fe*5270, *Fe*5335,*Fe*5406, *Fe*5709, *Fe*5782, *NaI*,*NaD*) for an accurate reconstruction of the physical properties of the target galaxies. We performed this calculation on the binned MUSE data using an in-house python software that performs the necessary corrections to obtain index strengths in the Lick system (resolution $= 220$ km s^{-1}) taking into account the broadening of the lines due to the galaxy dispersion. A MonteCarlo approach has been used to derive reliable uncertainties on the line indices. We compared our results with the literature

measurements available for NGC 7619 (Pu et al. 2010). We obtain a good agreement with their values and their radial profiles despite a slightly lower velocity dispersion than previously found in the galaxy core. This variation might be due to the high quality 2D data provided by MUSE.

We than interpreted the observations of the line indices using three different stellar population models in order to derive the radial variations of the physical properties of the two galaxies in the sample. These properties include the age of the stellar population, the metal content, the abundance of α elements compared to the total metal content, and the shape of the stellar initial mass function. The first of these models is the Thomas et al. (2005), from which we have been able to evaluate, for a fixed Kroupa IMF, the radial profiles of age, metallicity, α/Fe, and M/L for our galaxies. The second model from Conroy et al. (2009) allows us, for a fixed solar abundance to study the radial profile of the IMF. Lastly, using the Conroy & van Dokkum (2012) models, we studied the impact of different α/Fe on the line strengths assuming fixed age of 13.5 Gyr and solar metallicity, we found that the NaI index is very sensitive to the slope of the IMF in in the regime of dwarf stars ($0.08M_{\odot} < M < 0.5M_{\odot}$). However this index does also change significantly as a function of metallicity and overabundance.

From the fits we found two old, metal rich and over abundant galaxies, and a broad consistency with a Kroupa IMF in the inner parts. This is in agreement with previous measurements from Rusli et al. (2013) for NGC 7619 and from Rusli et al. (2011) for NGC 1332 and with dynamical models.

To further improve this thesis project, in the future, we need more advanced stellar population models that allow us to freely and self consistently choose the metallicity, α overabundance, Age, and IMF shape when generating the syntetic spectra. We would also benefit from deeper and well calibrated observations in the near-infrared bands (IZ and YJ from the KMOS instrument) to access other IMF sensitive indices (on top of the NaI) like the FeH band (see Alton et al. 2017). In conclusion, very tight reconstructions of the IMF shapes will strongly constrain the radial dependence of the mass-to-light ratio, a quantity which is of critical importance in dynamical models of these galaxies. From these models it is possible to statistically reconstruct the orbits of stars which can be compared to photometric and spectroscopic observations, to achieve constraints on the importance of dark matter and black holes in the inner regions of giant Early-Type galaxies.

Bibliography

Alton, P. D., Smith, R. J., & Lucey, J. R. 2017, MNRAS, 468, 1594

Barth, A. J., Boizelle, B., Darling, J. K., et al. 2016, in American Astronomical Society Meeting Abstracts, Vol. 228, American Astronomical Society Meeting Abstracts #228, 103.05

Bender, R., Doebereiner, S., & Moellenhoff, C. 1988, A&AS, 74, 385

Cappellari, M. 2012, in Dynamics Meets Kinematic Tracers, 30

Cappellari, M. 2016, ARA&A, 54, 597

Cappellari, M. 2017, MNRAS, 466, 798

Cappellari, M. & Copin, Y. 2003, Monthly Notices of the Royal Astronomical Society, 342, 345

Cappellari, M. & Emsellem, E. 2004, PASP, 116, 138

Conroy, C., Dutton, A. A., Graves, G. J., Mendel, J. T., & van Dokkum, P. G. 2013, ApJ, 776, L26

Conroy, C., Gunn, J. E., & White, M. 2009, ApJ, 699, 486

Conroy, C. & van Dokkum, P. G. 2012, ApJ, 760, 71

Davies, R. I., Agudo Berbel, A., Wiezorrek, E., et al. 2013, A&A, 558, A56

de Vaucouleurs, G., de Vaucouleurs, A., Corwin, Jr., H. G., et al. 1991, Third Reference Catalogue of Bright Galaxies. Volume I: Explanations and references. Volume II: Data for galaxies between 0^h and 12^h. Volume III: Data for galaxies between 12^h and 24^h.

Faber, S. M., Friel, E. D., Burstein, D., & Gaskell, C. M. 1985, ApJS, 57, 711

Girardi, L., Bressan, A., Bertelli, G., & Chiosi, C. 2000, A&AS, 141, 371

Kormendy, J. & Bender, R. 2009, ApJ, 691, L142

Lauer, T. R., Gebhardt, K., Faber, S. M., et al. 2007, ApJ, 664, 226

Magoulas, C., M. Springob, C., Colless, M., et al. 2012, 427

Mazzalay, X., Thomas, J., Saglia, R. P., et al. 2016, MNRAS, 462, 2847

Polletta, M., Tajer, M., Maraschi, L., et al. 2007, ApJ, 663, 81

Pu, S. B., Saglia, R. P., Fabricius, M. H., et al. 2010, A&A, 516, A4

Rembold, S. B., Pastoriza, M. G., Ducati, J. R., Rubio, M., & Roth, M. 2002, A&A, 391, 531

Rusli, S. P., Thomas, J., Erwin, P., et al. 2011, MNRAS, 410, 1223

Rusli, S. P., Thomas, J., Saglia, R. P., et al. 2013, AJ, 146, 45

Smette, A., Sana, H., Noll, S., et al. 2015, A&A, 576, A77

Thomas, D., Maraston, C., Bender, R., & Mendes de Oliveira, C. 2005, ApJ, 621, 673

Thomas, J., Saglia, R., Bender, R., Erwin, P., & Fabricius, M. 2015, in IAU Symposium, Vol. 311, Galaxy Masses as Constraints of Formation Models, ed. M. Cappellari & S. Courteau, 36–39

Thomas, J., Saglia, R. P., Bender, R., Erwin, P., & Fabricius, M. 2014, The Astrophysical Journal, 782, 39

Thomas, J., Saglia, R. P., Bender, R., et al. 2011, MNRAS, 415, 545

Trager, S. C., Faber, S. M., Worthey, G., & González, J. J. 2000, AJ, 119, 1645

Wegner, G., Bernardi, M., Willmer, C. N. A., et al. 2003, AJ, 126, 2268

Worthey, G., Faber, S. M., Gonzalez, J. J., & Burstein, D. 1994, ApJS, 94, 687

Worthey, G. & Ottaviani, D. L. 1997, ApJS, 111, 377

Acknowledgments

I would like to thank all my supervisors and co-supervisors that make this work possible. First Prof. Andrea Cimatti, that allow me to begin this journey. Then I like to thank Prof. Roberto Saglia and Alessandra Beifiori, for carefully supervising and guide me through this work. Finally I'd like to thank to thank Matteo Fossati for keeping always his door open for me and for everything he patiently taught me.

Durante gli anni di crescita che hanno caratterizzato questo percorso, ho scritto mentalmente questi ringraziamenti molte volte. Le persone e il modo in cui lo hanno influenzato si è evoluto nel tempo, ma alcune di queste mi hanno accompagnato in tutto questo tragitto e hanno lasciato un contributo importante. Prima di tutto ci tengo a ringraziare i miei genitori e mia sorella, che durante tutti questi anni mi hanno sempre sostenuto, anche più di quanto fosse ragionevole, permettondomi esplorare varie strade e di formarmi per come sono. Senza di loro questo percorso non sarebbe stato solo impraticabile, ma non mi avrebbe lasciato tutti gli insegnamenti e i valori che loro invece hanno saputo trasmettermi. Sanno già di avere un posto speciale Pacci,Fede, Ceci, Stanz, Acco, Pindro,Tommy, Gio, Giulia, Tommaso, Jacopo, Matteo e Elena, e sanno che tutto il bene, l'affetto e il sostegno reciproco lo abbiamo dimostrato, stiamo continuando a dimostrarlo e lo dimostreremo al di là di quanto possa esprimere in queste righe. Infine voglio ringraziare Elena, per tutto quello che ha fatto al di dentro e soprattutto al di fuori di questo percorso e per tutto quello che ha costruito insieme a me durante.